

Article

Effect of a Large Proton Exchange Membrane Electrolyser on Power System Small-Signal Angular Stability

Guy Wanlongo Ndiwulu *, Eduardo Vasquez Mayen * and Emmanuel De Jaeger

Mechatronic, Electrical Energy, and Dynamic Systems, UCLouvain, 1348 Louvain-la-Neuve, Belgium; emmanuel.dejaeger@uclouvain.be

* Correspondence: guy.wanlongo@uclouvain.be (G.W.N.); eduardo.vasquez@uclouvain.be (E.V.M.)

Abstract: The dynamics of electrical systems have changed significantly with the increasing penetration of non-conventional loads such as hydrogen electrolysers. As a result, detailed investigations are required to quantify and characterize these loads' effects on the dynamic response of interconnected synchronous machines after being subjected to a disturbance. Many studies have focused on the effects of conventional static and dynamic loads. However, the impact of hydrogen electrolysers on the stability of power systems' rotor angles is rarely studied. This paper assesses the effect of proton exchange membrane (PEM) electrolysers on small-disturbance rotor-angle stability. Dynamic modelling and the control of a PEM electrolyser as a load are first studied to achieve this. Then, the proposed electrolyser model is tested in the Amercoeur plant, which is part of the Belgian power system, to study its effect on the small-signal rotor-angle stability. Two approaches are considered to examine this impact: an analytical approach and time-domain simulations. The analytical approach consists of establishing a state-space model of the Belgian test system through linearisation around an operating point of the non-linear differential and the algebraic equations of the synchronous generators, the PEM electrolyser, the loads, and the network. The obtained state-space model allows for the determination of the eigenvalues, which are useful to evaluate the effect of the PEM electrolyser on the small-signal rotor-angle stability. This impact is investigated by examining the movement of the eigenvalues in the left complex half-plane. The obtained results show that the PEM electrolyser affects the electromechanical modes of synchronous machines by increasing their oscillation frequencies. The results also show that the effect of the electrolyser on these modes can be improved by adjusting the inertial constant and the damping coefficient of the synchronous machines. These results are consolidated through time-domain simulations using the software Matlab/Simscape from the version MatlabR2022a-academic use from Mathworks.

Keywords: PEM electrolyser; small-signal modelling; thyristor rectifier; rotor-angle stability



Citation: Wanlongo Ndiwulu, G.; Vasquez Mayen, E.; De Jaeger, E. Effect of a Large Proton Exchange Membrane Electrolyser on Power System Small-Signal Angular Stability. *Electricity* **2023**, *4*, 381–409. <https://doi.org/10.3390/electricity4040021>

Academic Editors: Da Xie, Yanchi Zhang, Dongdong Li, Chenghong Gu, Ignacio Hernando-Gil and Nan Zhao

Received: 5 October 2023

Revised: 3 November 2023

Accepted: 13 November 2023

Published: 1 December 2023



Copyright: © 2023 by the authors. Licensee MDPI, Basel, Switzerland. This article is an open access article distributed under the terms and conditions of the Creative Commons Attribution (CC BY) license (<https://creativecommons.org/licenses/by/4.0/>).

1. Introduction

Nowadays, hydrogen demand and production in a multitude of sectors are constantly increasing. As a result, the number of hydrogen electrolysers connected to transmission power systems is increasing. Hydrogen electrolysers are electrochemical devices used to separate water molecules into hydrogen and oxygen by passing a DC current through them [1]. This DC current is proportional to the hydrogen production. There are different hydrogen electrolyser technologies, which range from small systems (kilowatts) to large-scale systems (multiple megawatts) [1]. The most well-known technologies in industrial projects under development are alkaline electrolysers and proton exchange membrane (PEM) electrolysers [2]. Alkaline electrolyser technology, which is widely used today, is considered a mature technology in the industrial sector. Due to their advantages over alkaline electrolysers, such as high power density and cell efficiency, as well as fast dynamics, PEM electrolysers are in a period of great expansion and development for integration into power systems, including renewable energy production systems [1–5]. For this reason,

PEM electrolyser technology is dealt with within this paper. Hydrogen electrolysers can be viewed as flexible loads that can facilitate the large-scale integration of intermittent renewable sources into future power systems and provide power grid services [6,7]. As loads, hydrogen electrolysers can have an impact on the dynamics and stability of power systems. The use of power electronic converters as an interface for their integration into the grid can also affect the power quality and dynamics of power systems [8,9]. In addition, the dynamic response of the required electrolyser current to produce hydrogen can influence the dynamics of power systems. Detailed investigations of the impact of hydrogen electrolysers are required to characterize the dynamic response of the rotor-angle stability, frequency stability, and voltage stability. However, the majority of studies have focused mainly on frequency stability [3,5,6,10] and techno-economical aspects [10]. Few articles have dealt with the effect of hydrogen electrolysers on voltage stability [10], and the impact of electrolysers on rotor-angle stability has rarely been studied.

This paper focuses on the impact of a large-scale PEM electrolyser on a power system's small-signal rotor-angle stability. The small-disturbance rotor-angle stability can be defined as the capacity of a set of interconnected synchronous machines to maintain synchronism after being subjected to a small disturbance [11]. The dynamic responses of the set of interconnected synchronous machines are quantified and characterized to assess the influence of the PEM electrolyser on the power system dynamics. To this end, a large-scale PEM electrolyser project within the Belgian power system around Amercoeur is considered as a test system. Before investigating the effect of a hydrogen PEM electrolyser on the small-signal rotor-angle stability, we first identify the nature of PEM electrolysers when they are considered as loads within the power system, that is, whether a hydrogen PEM electrolyser can be regarded as a constant impedance load, a constant current load, or a constant power load. To achieve this, it is necessary to first model a hydrogen PEM electrolyser, then model the power electronic converter, and, finally, to develop a control structure for the power electronic converter to adjust the electrolyser current.

Concerning the dynamic modelling of PEM electrolysers, various electrochemical models are proposed in the literature [2,12–14]. The authors of reference [2] developed a dynamic electrical model of a PEM electrolyser, taking into account the dynamic behaviour of the PEM electrolyser during sudden variations in the input current. An equivalent electrical model of the PEM electrolyser with adaptive parameters for both static and dynamic operating conditions was proposed in [12]. The study reported in [12] focused on modelling cell voltage as a function of static and dynamic operations. In [14], an analytical–dynamic analysis model for a PEM electrolyser deduced from physical laws and electrochemical equations was proposed. The dynamic modelling of PEM electrolysers, as described in the literature, can be categorized into four groups based on various physical aspects, such as the required voltage (reversible voltage) for the electrolysis [15,16], activation overpotential, ohmic resistance, and the diffusion aspects at both the anode and the cathode. The activation overpotential represents the electrochemical kinetic behaviour [17]. It is therefore a representation of the speed of the reactions taking place on the electrode surface [17]. In contrast, ohmic overpotential is caused by the ohmic resistance of the electronic materials, such as current collectors, bipolar plates, and electrode surfaces [17]. It includes electron and proton conduction through the PEM. The electrochemical model of the PEM electrolyser investigated in [2,4,12,14,17] is referred to as the first model (*Model 1*) in this paper. *Model 1* is composed of the activation overpotential at the anode and cathode, membrane overpotential, and reversible potential. The activation overpotential at both the anode and cathode is modelled by two capacitor-resistance branches. Furthermore, the membrane overpotential is modelled by the ohmic overpotential. *Model 1* is one of the most studied models in dynamic modelling analysis of electrolysers. Nevertheless, its dynamic behaviour is often not studied. The second model (*Model 2*) considered in this paper includes a Warburg impedance at both the anode and the cathode, as proposed in [10]. The Warburg impedance is related to the concentration losses in the PEM electrolyser and is more important at low frequency and high current density [18,19]. However,

dynamic modelling of the electrochemical model related to *Model 2* is not proposed in the literature. Other authors have neglected the activation overpotential at the cathode, as in [3,4,8,10]. This is because the contribution of this overpotential is considered small compared to the contributions of the activation overpotential at the anode, the ohmic overpotential, and the reversible voltage. As a result, the electrochemical model without the activation overpotential of the cathode can be classified as either a model with a Warburg impedance (*Model 3*) or a model without a Warburg impedance (*Model 4*). The electrochemical model with Warburg impedance is often modelled by a Randles–Warburg cell, as depicted in [10,20]. *Model 3* includes a frequency-dependent Warburg element, which is parallel to a conventional capacitor, and a conventional resistor, which is in series with the Warburg element. The Warburg model brings the frequency-dependent characterizations of the resistor and capacitor, which modify the dynamic response of the cell voltage. *Model 4*, which does not consider the Warburg impedance, is described in [3,4,8]. As with the first two electrochemical models presented previously, the dynamic behaviour of the last two electrochemical models is also not examined in the literature. The dynamic responses of four models proposed in the literature are studied in this article in order to choose which one can be used in load modelling and small signal modelling. This choice is dictated by the time constant that characterizes the dynamic response of each model. For the model of the hydrogen PEM electrolyser, the temperature and pressure are considered to be constant, and the degradation of the catalyst and the membrane is not taken into account.

A 12-pulse thyristor rectifier is often used as interface to integrate hydrogen electrolyzers into the grid. Because this technology is one of the most mature and important solutions in high-power rectification applications [8], a current control structure is proposed to adjust the appropriate firing angle to achieve the desired electrolyser current. The proposed current control structure is established based on a dynamic model of the average model of the thyristor rectifier and of the proposed hydrogen PEM electrolyser model.

Finally, the effect of the PEM electrolyser model on the small-signal rotor-angle stability is studied using a state-space model and time-domain simulations of the test transmission system. The proposed state-space model is based on linearisation around an operating point of the non-linear differential and algebraic equations of the synchronous generators, the distribution network, the conventional loads, and the PEM electrolyser. In this approach, the synchronous generators and the network are modelled in the dq -synchronous reference frame. Then, all the components within the transmission network are translated into the common synchronous reference frame, rotating at a common frequency, as described in [21]. As well as consolidating the analytical results, time-domain simulations are also employed in this paper to study the impact of the proposed modelling of the electrolyser as a load. The contributions of this study can be summarized as follows:

- A dynamic model and a state-space model of a system formed by a PEM electrolyser and a 12-pulse thyristor rectifier is proposed.
- A control structure for the electrolyser current from the dynamic model of the PEM electrolyser and for the average model of the 12-pulse thyristor rectifier is proposed.
- A model of the PEM electrolyser as a load is proposed to identify whether it can be considered a constant impedance load, a constant current load, or a constant power load.
- We study the effects of the PEM electrolyser on the stability of the small-signal rotor-angle using analytical and time-domain simulation approaches.

The remainder of this paper is organized as follows: Section 2 presents the details of the proposed dynamic model for the PEM electrolyser, the thyristor rectifier, the proposed control structure of electrolyser current, and the modelling of the electrolyser as a load. Section 3 presents the details of the proposed small-signal model of the Belgian test system, while the stability analysis results are presented in Section 4. Finally, Section 5 concludes the paper.

2. Power System Architecture and Integration of Hydrogen PEM Electrolyser

Figure 1 describes the used test system, in which 100 MW of PEM electrolyzers are connected to the 150 kV busbar. It is the topology corresponding to the Belgian power system around the Amercoeur power plant. It consists of three synchronous generators (SGs) connected to the transmission grid through main Busbar 4, 6, and 11. The SGs are round rotor machines with static exciters. The three SGs are coupled with the thermal power plants. The dynamic of the primary source coupled with the SG is not studied in this article. It is assumed that the three SGs operate with constant power generated by the primary source. They are modelled as nodes with fixed active power (P) and reactive power (Q) (PQ node). The 270 MW synchronous generator (SG 1) is connected to Busbar 4, to which the PEM electrolyser is connected. The 150 MW generator (SG 2) is connected to the electrolyser via Busbar 6 and Busbar 5, while the 410 MW synchronous generator (SG 3) is connected to the electrolyser through Busbar 11, Busbar 10, and Busbar 5. A large 100 WM PEM electrolyser is connected to Busbar 4. The large-scale PEM electrolyser is assumed to be viewed as a large load by the power system, consuming only active power.

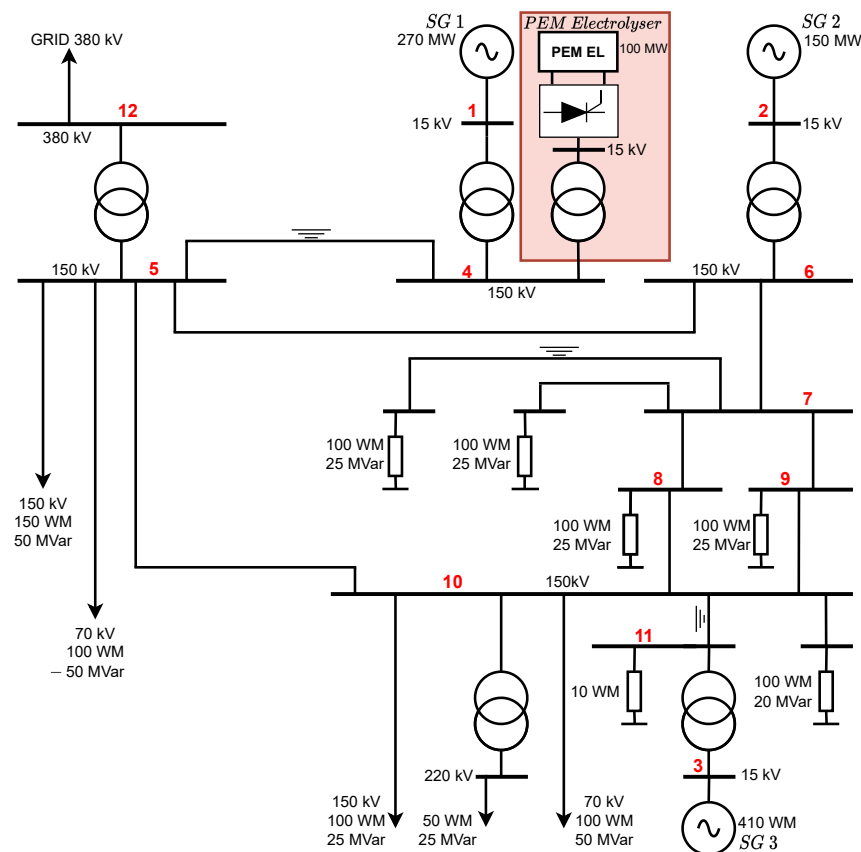


Figure 1. Test grid around the Belgian Amercoeur plant, in which 100 MW of PEM electrolyzers are connected to the grid through a 12-pulse thyristor rectifier. The number of each busbar is given in red.

2.1. Dynamic Modelling of the PEM Electrolyser

In order to model an electrolyser as a whole, it is necessary to look at each of its constituent aspects, such as electrochemical, electrical, thermal, mass transfer, and fluid [22] components. This paper focuses only on the electrochemical and electrical models.

Various electrochemical models of PEM electrolyzers have been proposed in the literature [2,3,8,10,12–14,20], which can be categorized into four groups, as discussed in the introduction: *Model 1*, *Model 2*, *Model 3*, and *Model 4*. The performance of each model can be quantified by evaluating the dynamic response of the cell voltage for a fixed cell

current. The dynamic behaviour of these four electrochemical models is obtained by the following equations:

- *Model 1*: Classical electrochemical model without Warburg impedance.

This model is described in [2,4,12,13,15,16], and the cell voltage across a PEM stack is given by

$$V_{cell} = V_{act,c} + V_{act,a} + R_m i_{cell} + V_{rev} \quad (1)$$

where $V_{act,a}$ and $V_{act,c}$ are the activation overpotential at the anode and at the cathode, respectively; i_{cell} represents the input current of the cell; and R_m and V_{rev} are the ohmic resistance and reverse voltage potential (reversible potential), respectively, during the water-splitting reaction. The dynamic behaviour of this classical electrochemical model is imposed by $V_{act,i}$, and it is modelled by:

$$\frac{dV_{act,c}}{dt} = \frac{i_{cell}}{C_{dl,c}} - \frac{V_{act,c}}{R_{ct,c}C_{dl,c}} \quad (2)$$

$$\frac{dV_{act,a}}{dt} = \frac{i_{cell}}{C_{dl,a}} - \frac{V_{act,a}}{R_{ct,a}C_{dl,a}} \quad (3)$$

where C_{dl_i} represents the double layer capacity, and $R_{ct,a}$ and $R_{ct,c}$ are the charge transfer resistances at the anode and cathode, respectively, which are temperature-dependent.

- *Model 2*: Classical electrochemical model with a Randles–Warburg cell.

This electrochemical model is presented in [10]. Its dynamic model is given by:

$$\frac{dV_{act,c}}{dt} = \frac{i_{cell}}{C_{dl,c}} - \frac{V_{act,c}}{(R_{ct,c} + Z_w)C_{dl,c}} \quad (4)$$

$$\frac{dV_{act,a}}{dt} = \frac{i_{cell}}{C_{dl,a}} - \frac{V_{act,a}}{(R_{ct,a} + Z_w)C_{dl,a}} \quad (5)$$

where Z_w denotes the Warburg impedance, which is frequency-dependent. Its mathematical expression is given as follows [19]:

$$Z_w = \frac{R_{d_1}}{1 + R_{d_1}C_{d_1}s} + \frac{R_{d_2}}{1 + R_{d_2}C_{d_2}s} \quad (6)$$

where $R_{d_i} = R_i R_d$, R_d , and R_i are the diffusion resistance and charge transfer resistance, respectively, and $C_{d_i} = C_{dli} \tau_d / R_d$, τ_d and C_{dli} represent the diffusion time constant and double layer capacitance, respectively.

- *Model 3*: Electrochemical model without the activation overpotential of the cathode and with Randles–Warburg impedance.

This model is presented in [10,20]. Without the activation overpotential at the cathode, the cell voltage across the PEM stack is modelled as follows:

$$V_{cell} = V_{act,a} + R_m i_{cell} + V_{rev} \quad (7)$$

The dynamic model of activation overpotential at the anode is modelled as in Equation (5).

- *Model 4*: Electrochemical model without activation overpotential at the cathode or a Warburg cell.

This model is depicted in [4,8]. The dynamic model of the cell voltage across the PEM electrolyser as a function of the activation overpotential at the anode is given by Equations (5) and (7). For a cell current set to 5 A, the dynamic responses of the cell voltages of *Model 1*, *Model 2*, *Model 3*, and *Model 4* from Equations (1)–(7) are described in Figure 2. The used cell parameters and Randles–Warburg cell parameters of those models are given in [10,18].

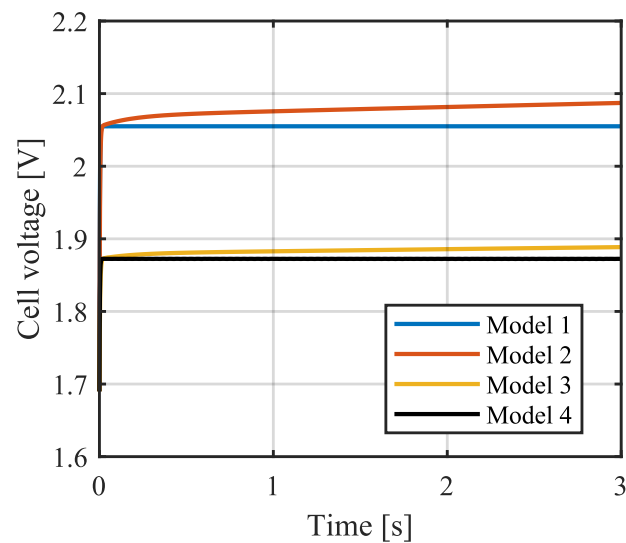


Figure 2. Dynamic response of the cell voltage of each of the four electrochemical models proposed in the literature as a function of the cell current. The cell input current is set to 5 A.

Figure 2 shows that the four electrochemical models can be identified in two groups: models without activation overpotential of the cathode (*Model 3* and *Model 4*) and complete models (*Model 1* and *Model 2*). For each group, we can identify models with Warburg impedance (*Model 2* and *Model 3*) and those without Warburg impedance (*Model 1* and *Model 4*). The impact of Warburg impedance on the cell voltage is also observed through the voltage deviation between *Model 2* and *Model 1* and that between *Model 3* and *Model 4*. Furthermore, the difference in voltage between the two groups is around 0.182 V, which represents the cathode activation overpotential. This overpotential is smaller than the total cell voltage, which is close to 2.055 V for *Model 1* and *Model 2* and around 1.872 V for *Model 3* and *Model 4* under steady-state conditions. This may be the reason why some authors neglected this cathode activation overpotential in their models [10].

Additionally, Figure 3 shows that the cell voltage responses of electrochemical models with Warburg impedance (*Model 2* and *Model 3*) are close to those without Warburg impedance (*Model 1* and *Model 4*). However, their transient response is higher than that of *Model 1* and *Model 4*. This is illustrated by the time constant, which is higher for *Model 2* and *Model 3* than for *Model 1* and *Model 4*.

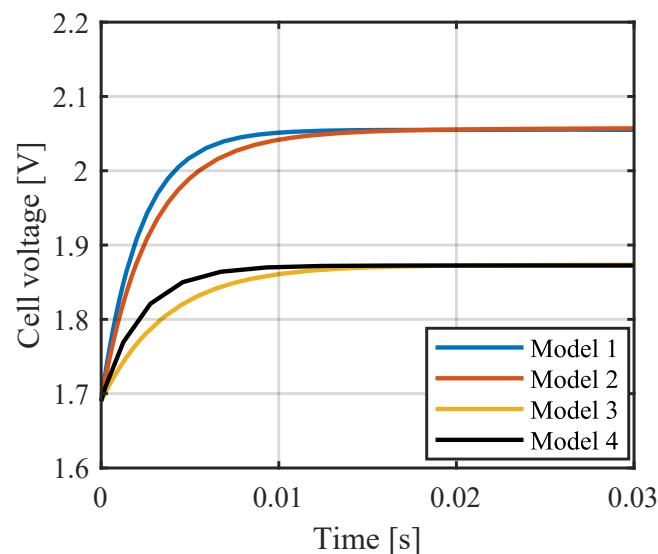


Figure 3. Transient response of the cell voltage of each of the four electrochemical models proposed in the literature as a function of the cell current. The cell input current is set to 5 A.

From these results, it can be concluded that the dynamic response of electrochemical models with a Warburg impedance (or a Randles–Warburg cell) is close to that of those without a Warburg impedance. Nevertheless, Warburg impedance can introduce a larger time constant in the transient response, and it can make the dynamic modelling of the electrochemical model more complex. Therefore, *Model 4* is used for the rest of this paper. *Model 4* offers a better transient response compared to the other models (see Figure 3).

2.2. Modelling of the 12-Pulse Thyristor Rectifier and the Electrolyser Current Controller

Figure 4 shows a hydrogen PEM electrolyser model connected to the grid through a 12-pulse thyristor rectifier and a three-winding wye-wye-delta transformer. The PEM electrolyser is modelled by the electrochemical model as described in the previous subsection. The three-winding transformer has the ability to eliminate the 5th- and 7th-order harmonic currents [8]. The electrolyser model is connected to the rectifier bridge via a filter inductance (L_f) and interphase inductances (L_{int}). The two 6-pulse thyristor rectifiers connected in parallel are used to form a 12-pulse thyristor rectifier. This configuration is often considered to be one of the most mature solutions for high-current rectification applications [8]. The operation of each six-pulse rectifier is ensured by a firing angle (α) that is either specified or generated by a controller, depending on the desired response of the rectifier DC side. Figure 4 also highlights that the transfer of active power (P_{AC}) from the AC side to the DC side (P_{DC}) is ensured by an appropriate firing-angle signal. The DC voltage and DC current are also related to the firing angle generated by the current controller from the current set point and the measurements of the DC current signal (i_{dc0}) and the AC voltage signal (V_{abc}). V_{abc} can be measured at the primary or secondary end of the three-winding transformer. It is used by the phase-locked loop (PLL) to synchronize the electrolyser with the grid frequency.

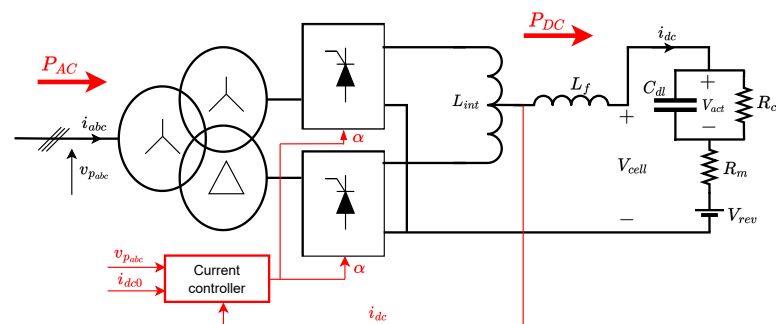


Figure 4. Hydrogen PEM electrolyser model connected to the grid through a 12-pulse thyristor rectifier.

2.2.1. Electrical Model of the 12-Pulse Thyristor Rectifier

Establishing the dynamic model shown in Figure 4 requires that all the parameters and variables on the AC side of the rectifier be brought back to the DC side. To do this, the average model of a 12-pulse thyristor rectifier can be considered. Additionally, the transformer is modelled by the primary and secondary leakage inductances.

Considering that the primary end of the transformer is supplied by U_p , this voltage can be seen by the electrolyser through the DC voltage using the following expression:

$$V_{dc} = 1.4 k U_p \cos \alpha \quad (8)$$

where U_p is the RMS phase-to-phase voltage at the primary end of the transformer, and k represents the ratio between the RMS phase-to-phase voltage at the secondary end of the transformer (U_s) and that at the primary voltage (U_p). Finally, α corresponds to the firing angle.

Equation (8) shows that the DC voltage is a function of the firing angle. It shows that the maximum voltage can be obtained when the firing angle is equal to zero. We assume that the transfer of current between two consecutive thyristors in a commutation

group takes a finite amount of time (overlap time). This overlap time depends on the phase-to-phase voltage between the thyristors participating in the commutation process, as well as the leakage inductance between the thyristor rectifier and the AC grid [23]. During the overlap time, the voltage and the current on the DC side are given by [23]:

$$V_{dc} = 1.4 k U_p [\cos\alpha + \cos(\alpha + \mu)] \quad (9)$$

$$I_{dc} = \frac{1.4 k}{\omega L_T} U_p [\cos\alpha - \cos(\alpha + \mu)] \quad (10)$$

where L_T is the leakage inductance of the transformer, and μ is the overlap angle. Equations (9) and (10) allow for the establishment of an equivalent circuit of the thyristor rectifier converter, as shown in Figure 5. The converter is modelled by a voltage source in series with a virtual resistance, whereas the overlap time phenomenon is modelled through the equivalent resistance given by $1.5\omega L_T/\pi$. Note that this resistance is not real (virtual resistance) because it does not dissipate power [23].

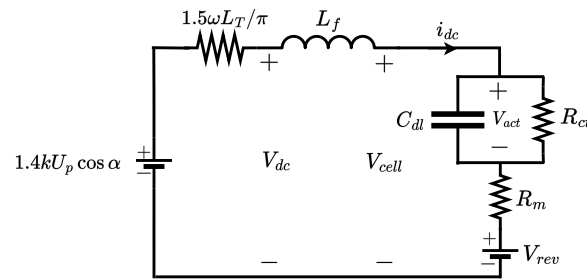


Figure 5. Electrical model of a PEM electrolyser and 12-pulse thyristor rectifier.

The dynamic model of the 12-pulse thyristor rectifier associated with the PEM electrolyser can be obtained from Figure 5 by applying Kirchhoff's law. The resulting model is defined as:

$$V_{cell} = 1.4 k U_p \cos\alpha - \frac{1.5\omega L_T}{\pi} i_{dc} - L_f \frac{di_{dc}}{dt} \quad (11)$$

$$V_{cell} = V_{rev} + R_m i_{dc} + V_{act} \quad (12)$$

$$C_{dl} \frac{dV_{act}}{dt} = i_{dc} - \frac{V_{act}}{R_{ct}} \quad (13)$$

2.2.2. Control Structure Model for the Electrolyser Current

The current control structure can be obtained from the dynamic model that is described by Equations (11) to (13). By applying Laplace transform to these equations and setting the initial conditions of current ($I_{dc}(0)$) and activation voltage ($V_{act}(0)$) to zero, the following is obtained:

$$V_{cell}(s) = 1.4 k U_p \cos\alpha - \frac{1.5\omega L_T}{\pi} I_{dc}(s) - s L_f I_{dc}(s) \quad (14)$$

$$V_{cell}(s) = V_{rev} + R_m I_{dc}(s) + V_{act}(s) \quad (15)$$

$$s C_{dl} V_{act}(s) = I_{dc}(s) - \frac{V_{act}(s)}{R_{ct}} \quad (16)$$

A block diagram of the system based on Equations (14) to (16) is shown in Figure 6. It describes the dynamic model of the PEM electrolyser associated with the 12-pulse thyristor rectifier in the s domain. This model is composed of two subloops of current and voltage, as well as signals of reverse voltage (V_{rev}) and DC input voltage ($1.4 U_s \cos(\alpha)$).

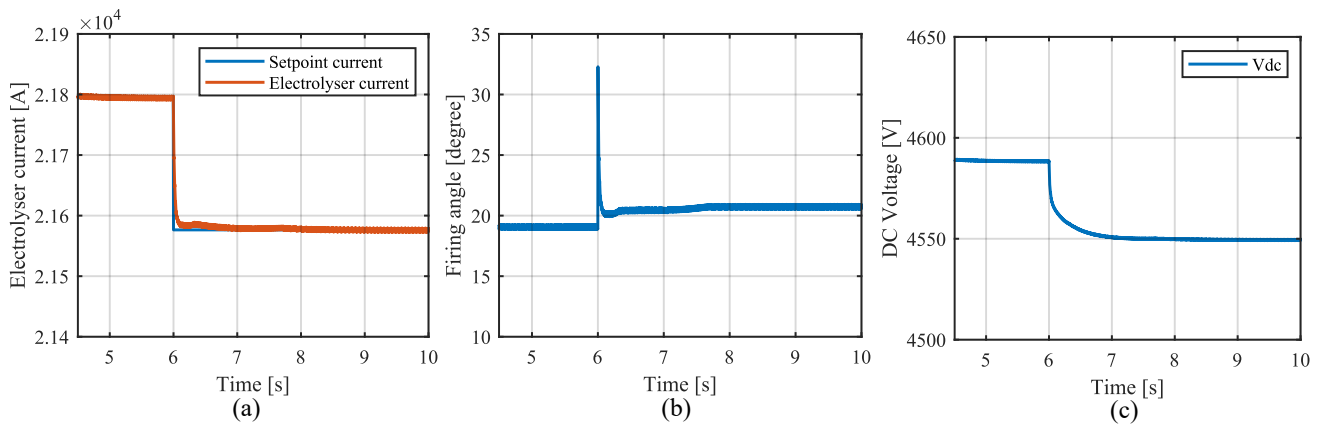


Figure 8. Steady-state conditions of the PEM electrolyser connected to *Busbar 4*: (a) DC electrolyser current; (b) firing angle; (c) DC voltage.

2.3. Modelling of the PEM Electrolyser as a Load

Consider the PEM electrolyser modelled in Figure 4, which is detailed in Figure 5. If one considers just the electrolyser part in Figure 5, the cell voltage of the stack is given by Equation (12). The activation voltage (V_{act}) is essentially caused by the voltage associated with the transfer resistance (R_{ct}) because the current on the capacitance is equal to zero. Therefore, one obtains:

$$V_{cell} = (R_m + R_{ct}) i_{dc} + V_{rev} \tag{17}$$

If it is assumed that there are no power losses between the grid and the electrolyser—that is to say that the active AC power P_{AC} supplied by the grid is equal to the DC power P_{DC} consumed by the hydrogen electrolyser—the power consumed by the electrolyser can be calculated as:

$$P_{AC} = P_{DC} = R_{eq} i_{dc}^2 + V_{rev} i_{dc}, \quad \text{with } R_{eq} = R_m + R_{ct} \tag{18}$$

Equation (18) shows that equivalent resistance (R_{eq}) and reversible potential (V_{rev}) are constant. This yields the active power (P_{AC}) as a function of the DC current (i_{dc}). P_{AC} is constituted by two active power terms ($R_{eq} i_{dc}^2$ and $V_{rev} i_{dc}$). The first element varies directly with the square of the current, while the latter varies with the current. In contrast to traditional static load modelling, the whole active power is modelled as a function of voltage magnitude. Since it is assumed that the DC voltage is fixed by the grid voltage to which the electrolyser is connected, the proposed modelling of the PEM electrolyser as load can be based on the controlled DC current. Thus, the PEM electrolyser can be modelled as a function of the cell current. According to Equation (18) and Figure 4, the PEM electrolyser can be modelled as a fraction of a constant impedance load combined with a fraction of a constant current load. The proposed model is expressed by Equation (19). In contrast to the conventional exponential ZIP model [25,26], the proposed model is modelled as a function of the current ratio instead of the voltage ratio. This makes the proposed load model of the electrolyser different from that of conventional constant impedance and constant current loads.

$$P = P_{E10} \left[a_1 \left(\frac{i_{dc}}{i_{dc0}} \right)^2 + a_2 \left(\frac{i_{dc}}{i_{dc0}} \right) \right] \tag{19}$$

where P_{E10} is the rated active power of the electrolyser, i_{dc0} represents the nominal DC electrolyser current related to the nominal active power of the electrolyser, i_{dc} is the controlled current of the electrolyser, a_1 represents the fraction of constant impedance load, and a_2 is the fraction of the constant current load.

Note that the modelling of the electrolyser as a load may depend on the model of the electrolyser, the technology of the power electronic converter, and the way in which the

electrolyser is connected to the grid. For a technology based on a single 12-pulse thyristor rectifier with n electrolysers connected in parallel on the DC side, as illustrated in Figure 9, the a_1 factor decreases with an increase in the number of parallel connected electrolyser models. Consequently, the PEM electrolyser behaves as a constant-current dominant load. Otherwise, it behaves as a constant-impedance dominant load.

Equations (18) and (19) and Figures 9 and 10 illustrate an example of the variation of fractions of a constant impedance load (a_1) and constant current load (a_2) depending on the number of electrolysers connected in parallel to the DC rectifier side. Four possibilities of connecting a 100 MW PEM electrolyser to the DC side of the 12-pulse thyristor rectifier are proposed. When one 100 MW PEM electrolyser model is connected to the DC side, Figure 10 shows that the fraction of constant impedance load (a_1) is higher than that of the constant current load (a_2). Therefore, the PEM electrolyser model can be seen by the grid as a dominant constant impedance load, whereas when two 50 MW PEM electrolysers are connected in parallel, this can be considered a dominant constant current load. For four models of 25 MW each connected in parallel, the fraction of constant impedance load (a_2) is higher than that of the constant current load (a_1). The PEM electrolyser can be assimilated to a dominant constant current load.

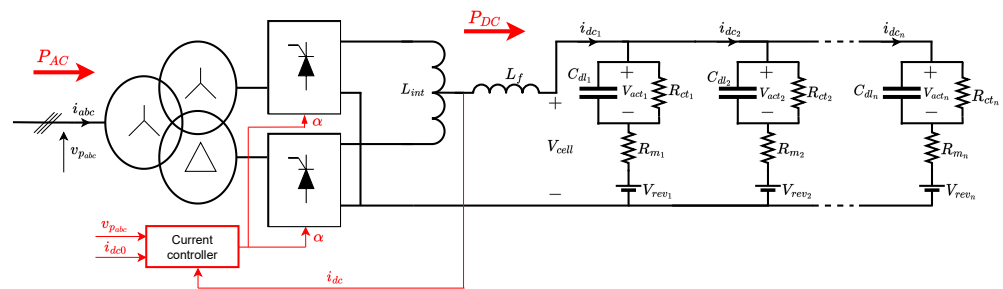


Figure 9. n PEM electrolyser models connected to the grid through a 12-pulse thyristor rectifier.

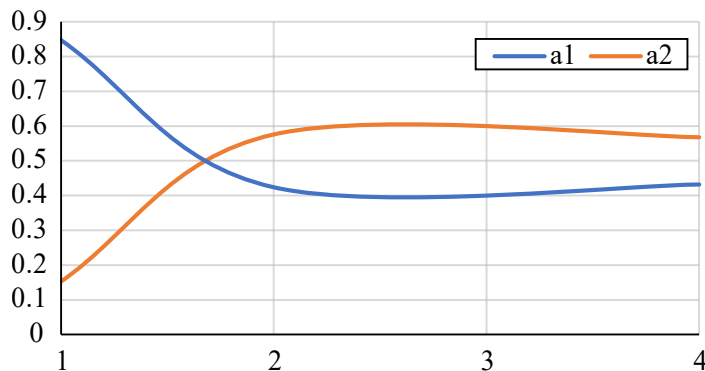


Figure 10. Fractions of constant impedance load and constant current load dependent on the number of electrolysers connected in parallel on the DC rectifier side.

3. Small-Signal Modelling of the Test System

Small-signal analysis was used as a tool to investigate the effects of the PEM electrolyser on the small-signal angular stability, i.e., to investigate the impact of the PEM electrolyser on the capacity of a set of interconnected synchronous machines to maintain synchronism after being subjected to a small disturbance. To do this, the power system shown in Figure 1 can be described by a system of non-linear differential and algebraic equations. Then, it is linearised around the operating point to obtain the state-space model of the grid. Hence, the state-space model of the grid shown in Figure 1 has to be established. It is composed of small-signal submodels of synchronous machines (270 MW, 150 MW, and 410 MW), static exciters, the PEM electrolyser, the network, and loads. Such equations can be written as follows.

3.1. State-Space Model of Synchronous Generators

The state-space model was obtained by the linearisation of non-linear differential and algebraic equations of the synchronous machines around an operational point. The rotor and stator equations are established in the dq reference frame (via Park transformation) [11,21]. The differential equations in the dq -synchronous reference frame of each synchronous machine connected to the grid are described by [21]:

$$\frac{d\delta_i}{dt} = \omega_i - \omega_s \quad (20)$$

$$\frac{d\omega_i}{dt} = \omega_s \frac{T_{M_i}}{2H_i} - \omega_s \frac{(E'_{q_i} - X'_{d_i} I_{d_i})}{2H_i} I_{q_i} - \omega_s \frac{(E'_{d_i} + X'_{q_i} I_{q_i})}{2H_i} I_{d_i} - \omega_s D_i \frac{\omega_i - \omega_s}{2H_i} \quad (21)$$

$$\frac{dE'_{q_i}}{dt} = -\frac{E'_{q_i}}{T'_{d_{o_i}}} - \frac{(X_{d_i} - X'_{d_i})}{T'_{d_{o_i}}} I_{d_i} + \frac{E_{f_{d_i}}}{T'_{d_{o_i}}} \quad \text{with} \quad E'_{q_i} = \frac{X_{m_{d_i}}}{X_{f_{d_i}}} \psi_{f_{d_i}} \quad (22)$$

$$\frac{dE'_{d_i}}{dt} = -\frac{E'_{d_i}}{T'_{q_{o_i}}} + \frac{I_{q_i}}{T'_{q_{o_i}}} (X_{q_i} - X'_{q_i}) \quad \text{with} \quad E'_{d_i} = -\frac{X_{m_{q_i}}}{X_{1_{q_i}}} \psi_{1_{q_i}} \quad (23)$$

where $i = 1, 2$, and 3 correspond to the number of the synchronous generator (SG 1, SG 2, and SG 3, respectively) connected to the test system; ω_s is the synchronous angular speed of the rotor; and ω_i and $\delta_i = \theta_i - \theta_s$ are the rotor speed and relative rotor angle, respectively. The rotor angle (θ_i) is measured with respect to the synchronously rotating frame of the constant base frequency (ω_b) and satisfies $d\theta_i/dt = \omega_b \omega_i$ [27]. T_{M_i} is the mechanical torque. D_i is the damping torque coefficient. H_i represents the inertial constant. I_{d_i} and I_{q_i} are the current components along the direct axis (d axis) and quadrature axis (q -axis), respectively. X_{d_i} and X_{q_i} are the synchronous reactances along the d axis and q axis, respectively. $T'_{d_{o_i}}$ and $T'_{q_{o_i}}$ are the transient time constants along the d axis and q axis, respectively. X'_{d_i} and X'_{q_i} represent the transient reactances along the d axis and q axis, respectively. $E_{f_{d_i}}$ is the field voltage. $\psi_{1_{q_i}}$ represents damper-winding ($1q$) flux linkages. $X_{1_{q_i}}$ is the damper-winding ($1q$) reactance. $X_{m_{d_i}}$ and $X_{m_{q_i}}$ are the magnetizing reactances in d -axis and q -axis, respectively. $X_{f_{d_i}}$ is the field d -axis reactance. E'_{d_i} is proportional to the rotor field flux along the d axis, while E'_{q_i} is proportional to the damper-winding flux along the q axis.

Each synchronous machine of the test system is composed of a static exciter to maintain a constant terminal voltage. The dynamic model of the static exciter is expressed according to the following equation [21]:

$$\frac{dE_{f_{d_i}}}{dt} = -\frac{1}{T_{A_i}} E_{f_{d_i}} + \frac{K_{A_i}}{T_{A_i}} (V_{ref_i} - V_i) \quad (24)$$

The real parts of the equations of the stator for each synchronous generator (SG, $i = 1, 2$, and 3) are given by [21]:

$$E'_{d_i} - V_i \sin(\delta_i - \theta_i) - R_{s_i} I_{d_i} + X'_{q_i} I_{q_i} = 0 \quad (25)$$

$$E'_{q_i} - V_i \cos(\delta_i - \theta_i) - R_{s_i} I_{q_i} + X'_{d_i} I_{d_i} = 0 \quad (26)$$

To obtain a linearised model for Equations (20)–(26), a small perturbation around the operating point is superimposed on the state variables δ_i , ω_i , E'_{d_i} , E'_{q_i} , $E_{f_{d_i}}$, I_{q_i} , I_{d_i} , V_i , V_{ref_i} , T_{M_i} , and θ_i , such as:

$$\begin{aligned} \delta_i &= \delta_{0_i} + \Delta\delta_i; \quad \omega_i = \omega_{0_i} + \Delta\omega_i; \quad E'_{q_i} = E'_{q_{0_i}} + \Delta E'_{q_i}; \quad E'_{d_i} = E'_{d_{0_i}} + \Delta E'_{d_i}; \\ E_{f_{d_i}} &= E_{f_{d_{0_i}}} + \Delta E_{f_{d_i}}; \quad I_{q_i} = I_{q_{0_i}} + \Delta I_{q_i}; \quad I_{d_i} = I_{d_{0_i}} + \Delta I_{d_i}; \quad V_i = V_{0_i} + \Delta V_i; \\ V_{ref_i} &= V_{ref_{0_i}} + \Delta V_{ref_i}; \quad T_{M_i} = T_{M_{0_i}} + \Delta T_{M_i}; \quad \text{and} \quad \theta_i = \theta_{0_i} + \Delta\theta_i. \end{aligned}$$

where δ_{0_i} , ω_{0_i} , E'_{d0_i} , E'_{q0_i} , E_{fd0_i} , I_{q0_i} , I_{d0_i} , V_{0_i} , V_{ref0_i} , T_{M0_i} , and θ_{0_i} represent the nominal values of the rotor angle, rotor speed, damper winding flux, rotor field flux, field voltage, q -axis current, d -axis current, terminal voltage of the SG, reference voltage of the exciter, mechanical torque, and voltage angle at bus i , respectively. $\Delta\delta_i$, $\Delta\omega_i$, $\Delta E'_{d_i}$, $\Delta E'_{q_i}$, ΔE_{fd_i} , ΔI_{q_i} , ΔI_{d_i} , ΔV_i , ΔV_{ref_i} , ΔT_{M_i} , and $\Delta\theta_i$ are the small disturbances of the state variables mentioned above.

By substituting the small disturbances defined above around the operating point in Equations (20) to (26) and neglecting the second and higher-order powers of the small perturbation and of the input vector in the Taylor-series expression, the state-space model of three synchronous machines was defined according to the following equations:

$$\Delta\dot{X} = A_{SG}\Delta X + B_{SG1}\Delta I_g + B_{SG2}\Delta V_g + B_{SG3}\Delta U \tag{27}$$

$$0 = C_{SG1}\Delta X + D_{SG1}\Delta I_g + D_{SG2}\Delta V_g \tag{28}$$

where $\Delta X = [\Delta X_1 \ \Delta X_2 \ \Delta X_3]^T$ represents the state vector composed of the state subvector of each synchronous generator connected to the test system. They are defined by $\Delta X_i = [\Delta\delta_i \ \Delta\omega_i \ \Delta E'_{q_i} \ \Delta E'_{d_i} \ \Delta E_{fd_i}]^T$. ΔI_g is the vector matrix of current components of the SG i along the d axis and q axis. It is expressed by $\Delta I_g = [\Delta I_{d1} \ \Delta I_{d2} \ \Delta I_{d3} \ \Delta I_{q1} \ \Delta I_{q2} \ \Delta I_{q3}]^T$. ΔV_g represents the vector matrix of voltage magnitude and the angle of the synchronous generator bus. It is defined by $\Delta V_g = [\Delta\theta^T \ \Delta V^T]^T$, where $\Delta\theta = [\Delta\theta_1 \ \Delta\theta_2 \ \Delta\theta_3]^T$ and $\Delta V = [\Delta V_1 \ \Delta V_2 \ \Delta V_3]^T$. $\Delta U = [\Delta T_M^T \ \Delta V_{ref}^T]^T$ is the input matrix of SG i , where $\Delta T_M = [\Delta T_{M1} \ \Delta T_{M2} \ \Delta T_{M3}]^T$ and $\Delta V_{ref} = [\Delta V_{ref1} \ \Delta V_{ref2} \ \Delta V_{ref3}]^T$. Matrices A_{SG} , B_{SG1} , B_{SG2} , B_{SG3} , C_{SG1} , D_{SG1} , and D_{SG2} are expressed as:

$$A_{SG} = \begin{bmatrix} A_{SG1} & 0 & 0 \\ 0 & A_{SG1} & 0 \\ 0 & 0 & A_{SG1} \end{bmatrix}_{15 \times 15}, \text{ where } A_{SG_i} = \begin{bmatrix} 0 & 1 & 0 & 0 & 0 \\ 0 & -\frac{D_i\omega_s}{2H_i} & -\frac{I_{q_i}\omega_s}{2H_i} & -\frac{I_{d_i}\omega_s}{2H_i} & 0 \\ 0 & 0 & -\frac{1}{T'_{d0_i}} & 0 & \frac{1}{T'_{d0_i}} \\ 0 & 0 & 0 & -\frac{1}{T'_{q0_i}} & 0 \\ 0 & 0 & 0 & 0 & -\frac{1}{T_{A_i}} \end{bmatrix};$$

$$B_{SG1} = \begin{bmatrix} B_{SG11} & 0 & 0 \\ 0 & B_{SG12} & 0 \\ 0 & 0 & B_{SG13} \end{bmatrix}_{15 \times 6}, \text{ where } B_{SG1_i} = \begin{bmatrix} 0 & 0 \\ \frac{X'_{d_i}I_{q_i} - E'_{d_i} - X'_{q_i}I_{q_i}}{2H_i} \omega_s & \frac{-E'_{q_i} + X'_{d_i}I_{d_i} - X'_{q_i}I_{d_i}}{2H_i} \omega_s \\ -\frac{X_{d_i} - X'_{d_i}}{T'_{d0_i}} & 0 \\ 0 & -\frac{X_{q_i} - X'_{q_i}}{T'_{q0_i}} \\ 0 & 0 \end{bmatrix};$$

$$B_{SG2} = \begin{bmatrix} B_{SG21} & 0 & 0 \\ 0 & B_{SG22} & 0 \\ 0 & 0 & B_{SG23} \end{bmatrix}_{15 \times 6}, \text{ where } B_{SG2_i} = \begin{bmatrix} 0 & 0 & 0 & 0 & -\frac{K_{A_i}}{T_{A_i}} \\ 0 & 0 & 0 & 0 & 0 \end{bmatrix}^T;$$

$$B_{SG3} = \begin{bmatrix} B_{SG31} & 0 & 0 \\ 0 & B_{SG32} & 0 \\ 0 & 0 & B_{SG33} \end{bmatrix}_{15 \times 6}, \text{ where } B_{SG3_i} = \begin{bmatrix} 0 & 0 & 0 & 0 & -\frac{K_{A_i}}{T_{A_i}} \\ 0 & \frac{\omega_s}{2H_i} & 0 & 0 & 0 \end{bmatrix}^T;$$

$$C_{SG1} = \begin{bmatrix} C_{SG11} & 0 & 0 \\ 0 & C_{SG12} & 0 \\ 0 & 0 & C_{SG13} \end{bmatrix}_{6 \times 15}, \text{ where } C_{SG1_i} = \begin{bmatrix} -V_i \cos(\delta_i - \theta_i) & 0 & 0 & 1 & 0 \\ V_i \sin(\delta_i - \theta_i) & 0 & 1 & 0 & 0 \end{bmatrix};$$

$$D_{SG1} = \begin{bmatrix} D_{SG11} & 0 & 0 \\ 0 & D_{SG12} & 0 \\ 0 & 0 & D_{SG13} \end{bmatrix}_{6 \times 6}, \text{ where } D_{SG1i} = \begin{bmatrix} -R_{s_i} & X'_{q_i} \\ -X'_{d_i} & -R_{s_i} \end{bmatrix}; \text{ and}$$

$$D_{SG2} = \begin{bmatrix} D_{SG21} & 0 & 0 \\ 0 & D_{SG22} & 0 \\ 0 & 0 & D_{SG23} \end{bmatrix}_{6 \times 6}, \text{ where } D_{SG2i} = \begin{bmatrix} V_i \cos(\delta_i - \theta_i) & -\sin(\delta_i - \theta_i) \\ -V_i \sin(\delta_i - \theta_i) & -\cos(\delta_i - \theta_i) \end{bmatrix}.$$

3.2. State-Space Model of the Electrolyser (EL)

According to Figure 4, the small-signal model of a set of electrolysers and the average model of a 12-pulse thyristor rectifier can be built around the state variable of current (i_{dc}) and the required firing angle (α) of the thyristor rectifier. By linearising Equation (18) around the operating point and by neglecting the second-order term of Δi_{dc} , one obtains:

$$\Delta P_{EL} = (2R_{eq}i_{dc0} + V_{rev})\Delta i_{dc} \tag{29}$$

Considering the current control structure around the proportional–integral (PI) controller as described in Figure 11, the firing angle can be written as a function of the parameters of the PI controller as:

$$\alpha = K_p(i_{dc0} - i_{dc}) + K_i(i_{dc0} - i_{dc}) \tag{30}$$

where K_p , K_i , and i_{dc0} represent the gain of the proportional controller, the gain of the integral controller, and the nominal current of hydrogen electrolyser, respectively.

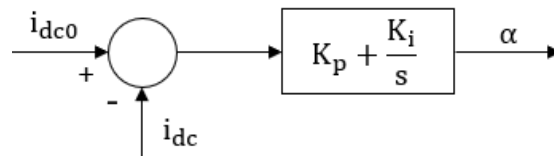


Figure 11. Firing angle associated with the parameters of the proportional-integral controller.

Linearisation of Equation (30) around the operating point, considering a nominal firing angle (α_0) of zero, yields:

$$\Delta \alpha = -(K_p + K_i)\Delta i_{dc} \tag{31}$$

The state-space model of the active and reactive power consumed by the PEM electrolyser can be expressed as:

$$\begin{bmatrix} \Delta P_{EL} \\ \Delta Q_{EL} \end{bmatrix} = \begin{bmatrix} 2R_{eq}i_{dc0} + V_{rev} & 0 \\ 0 & 0 \end{bmatrix} \begin{bmatrix} \Delta i_{dc} \\ \Delta \alpha \end{bmatrix} \tag{32}$$

According to Equations (11)–(13) and Figure 4, the voltage across the capacitance (C_{dl}) is equal to zero. Because it is seen as smoothing capacitance by the charge transfer resistance (R_{ct}), by substituting Equations (12) and (13) into Equation (11), one obtains:

$$\frac{di_{dc}}{dt} = -\left(R_m + R_{ct} + \frac{1.5\omega L_T}{\pi}\right)\frac{i_{dc}}{L_f} + \frac{1.4U_s \cos \alpha}{L_f} - \frac{V_{rev}}{L_f} \tag{33}$$

Thus, linearisation of Equation (33) around the operating point yields:

$$\Delta \dot{i}_{dc} = A_{EL}\Delta i_{dc} + B_{EL}\Delta \alpha \tag{34}$$

where $A_{EL} = -\frac{1}{L_f}\left(R_m + R_{ct} + \frac{1.5\omega L_T}{\pi}\right)$ and $B_{EL} = -\frac{1.4U_s \sin \alpha_0}{L_f}$. Meanwhile, α_0 is the firing angle related to steady-state conditions. Equations (31) and (34) describe the state-space model of the PEM electrolyser as a function of the gains of the controller, the parameters of the electrochemical model, and the grid voltage magnitude.

3.3. State-Space Model of the Network and Conventional Loads

The network equations for an n -bus system can be expressed in complex form as described in [21]. They are defined in two groups, namely equations associated with the generator buses and those associated with the load buses. It is assumed in this paper that the PEM electrolyser is connected to the generator bus. The constant power loads are connected to the load buses and to the generator buses. The network equations for the three generator buses (1, 2, and 3; see Figure 1) are defined as:

$$P_{G_i} + jQ_{G_i} + P_{L_i}(V_i) + jQ_{L_i}(V_i) + P_{EL}(i_{cell}) = \sum_{k=1}^n V_i V_k Y_{ik} [\cos(\theta_i - \theta_k - \beta_{ik}) + j\sin(\theta_i - \theta_k - \beta_{ik})] \quad (35)$$

with $P_{G_i} = I_{d_i} V_i \sin(\delta_i - \theta_i) + I_{q_i} V_i \cos(\delta_i - \theta_i)$ and $Q_{G_i} = I_{d_i} V_i \cos(\delta_i - \theta_i) - I_{q_i} V_i \sin(\delta_i - \theta_i)$, where P_{G_i} and Q_{G_i} are the active power and reactive power injected into bus i due to generator i ($i = 1, 2$, and 3), respectively. Equation (35) shows that for the generator buses, the active (P_{L_i}) and reactive (Q_{L_i}) powers of the constant power loads depend on the voltage magnitudes of the buses, while the active power of the electrolyser (P_{EL}) depends on the cell current. The power-balance form of Equation (35) is expressed as:

$$I_{d_i} V_i \sin(\delta_i - \theta_i) + I_{q_i} V_i \cos(\delta_i - \theta_i) + P_{L_i}(V_i) + P_{EL}(i_{cell}) - \sum_{k=1}^n V_i V_k Y_{ik} \cos(\theta_i - \theta_k - \beta_{ik}) = 0 \quad (36)$$

$$I_{d_i} V_i \cos(\delta_i - \theta_i) - I_{q_i} V_i \sin(\delta_i - \theta_i) + Q_{L_i}(V_i) - \sum_{k=1}^n V_i V_k Y_{ik} \sin(\theta_i - \theta_k - \beta_{ik}) = 0 \quad (37)$$

The network equations for the n -load buses (see Figure 1) are expressed in Equation (38). As assumed, only constant power loads are connected to the load buses. These are modelled by considering only the active power ($P_{L_i}(V_i)$) and reactive power ($Q_{L_i}(V_i)$).

$$P_{L_i}(V_i) + jQ_{L_i}(V_i) = \sum_{k=1}^n V_i V_k Y_{ik} [\cos(\theta_i - \theta_k - \alpha_{ik}) + j\sin(\theta_i - \theta_k - \beta_{ik})] \quad (38)$$

The power-balance form of Equation (38) is expressed as

$$P_{L_i}(V_i) - \sum_{k=1}^n V_i V_k Y_{ik} \cos(\theta_i - \theta_k - \beta_{ik}) = 0 \quad (39)$$

$$Q_{L_i}(V_i) - \sum_{k=1}^n V_i V_k Y_{ik} \sin(\theta_i - \theta_k - \beta_{ik}) = 0 \quad (40)$$

The state-space model of the generator buses is given by Equation (41). It is obtained by linearising Equations (36) and (37) around the operating point and by neglecting all the second-order terms associated with the small variations.

$$0 = C_{SGEL} \Delta X_{SGEL} + D_{SG3} \Delta I_g + D_{SG4} \Delta V_g + D_{NET1} \Delta V_{NET1} \quad (41)$$

where $\Delta X_{SGEL} = [\Delta X_1 \ \Delta X_2 \ \Delta X_3 \ \Delta X_{EL}]^T$ is the state vector of generators and of the electrolyser connected to the generator buses, $\Delta X_{EL} = \Delta i_{dc}$ represents the state variable of the electrolyser, and $\Delta V_{NET} = [\Delta \theta^T \ \Delta V^T]^T$ is the vector matrix formed by the voltage magnitude and angle submatrices of the network buses, where $\Delta \theta = [\Delta \theta_1 \ \Delta \theta_2 \ \dots \ \Delta \theta_m]^T$ represents the angle submatrix of the network buses, and $\Delta V = [\Delta V_1 \ \Delta V_2 \ \dots \ \Delta V_m]^T$ is the voltage magnitude submatrix of the network buses. m represents the non-generator buses, C_{SGEL} is the observation matrix, as expressed by:

$$C_{SGEL} = \begin{bmatrix} C_{SGEL1} & 0 & 0 \\ 0 & C_{SGEL2} & 0 \\ 0 & 0 & C_{SGEL3} \end{bmatrix}_{6 \times 16}$$

where C_{SGEL_1} is the matrix associated with the generator *Busbar 4* and the PEM electrolyser, and C_{SGEL_2} and C_{SGEL_3} are the matrices associated with the generator (*Busbar 6*) and *Busbar 11* without PEM electrolyser, respectively. Matrices C_{SGEL_2} and C_{SGEL_3} have dimensions of 2×5 because they are part of the busbars without an electrolyser.

$$C_{SGEL_1} = \begin{bmatrix} I_{d_i} V_i \cos(\delta_i - \theta_i) - I_{q_i} V_i \sin(\delta_i - \theta_i) & 0 & 0 & 0 & 0 & 2R_{eq} i_{dc0} + V_{rev} \\ -I_{d_i} V_i \sin(\delta_i - \theta_i) - I_{q_i} V_i \cos(\delta_i - \theta_i) & 0 & 0 & 0 & 0 & 0 \end{bmatrix}$$

Matrices D_{SG3} , D_{SG4} , and D_{NET1} are the direct transmission matrices and are defined as:

$$D_{SG3} = \begin{bmatrix} D_{SG3_1} & 0 & 0 \\ 0 & D_{SG3_2} & 0 \\ 0 & 0 & D_{SG3_3} \end{bmatrix}_{6 \times 6} \quad \text{with } D_{SG3_i} = \begin{bmatrix} V_i \sin(\delta_i - \theta_i) & -V_i \cos(\delta_i - \theta_i) \\ V_i \cos(\delta_i - \theta_i) & -V_i \sin(\delta_i - \theta_i) \end{bmatrix};$$

$$D_{SG4} = \begin{bmatrix} D_{SG4_{11}} & D_{SG4_{12}} & D_{SG4_{13}} \\ D_{SG4_{21}} & D_{SG4_{22}} & D_{SG4_{23}} \\ D_{SG4_{31}} & D_{SG4_{32}} & D_{SG4_{33}} \end{bmatrix}_{6 \times 6}$$

where $D_{SG4_{ik}}$ is the submatrix associated with synchronous generator i ($i = 1, 2,$ and 3 SGs) and with the generator buses (k , where $k = 1, 2,$ and 3 generator buses). They are defined by:

$$D_{SG4_{11}} = \begin{bmatrix} A_{SG4_1} & B_{SG4_1} \\ C_{SG4_1} & D_{SG4_1} \end{bmatrix}, \text{ with}$$

$$A_{SG4_1} = -I_{d_1} V_1 \cos(\delta_1 - \theta_1) + I_{q_1} V_1 \sin(\delta_1 - \theta_1) + V_1 \sum_{k=1}^3 V_k Y_{1k} \sin(\theta_1 - \theta_k - \beta_{1k})$$

$$B_{SG4_1} = I_{d_1} \sin(\delta_1 - \theta_1) + I_{q_1} \cos(\delta_1 - \theta_1) - \sum_{k=1}^3 V_k Y_{1k} \sin(\theta_1 - \theta_k - \beta_{1k}) - V_1 Y_{1k} \cos(\theta_1 - \theta_k - \beta_{1k}) + \frac{\partial P_{L_1}(V_1)}{\partial V_1}$$

$$C_{SG4_1} = -I_{d_1} V_1 \sin(\delta_1 - \theta_1) + I_{q_1} V_1 \cos(\delta_1 - \theta_1) - V_1 \sum_{k=1}^3 V_k Y_{1k} \cos(\theta_1 - \theta_k - \beta_{1k})$$

$$D_{SG4_1} = I_{d_1} \cos(\delta_1 - \theta_1) - I_{q_1} \sin(\delta_1 - \theta_1) - \sum_{k=1}^3 V_k Y_{1k} \sin(\theta_1 - \theta_k - \beta_{1k}) - V_1 Y_{1k} \sin(\theta_1 - \theta_k - \beta_{1k}) + \frac{\partial Q_{L_1}(V_1)}{\partial V_1}$$

$$D_{SG4_{12}} = \begin{bmatrix} -V_1 V_2 Y_{12} \sin(\theta_1 - \theta_2 - \beta_{12}) & -V_1 Y_{12} \cos(\theta_1 - \theta_2 - \beta_{12}) \\ V_1 V_2 Y_{12} \cos(\theta_1 - \theta_2 - \beta_{12}) & -V_1 Y_{12} \sin(\theta_1 - \theta_2 - \beta_{12}) \end{bmatrix}$$

$$D_{SG4_{13}} = \begin{bmatrix} -V_1 V_3 Y_{13} \sin(\theta_1 - \theta_3 - \beta_{13}) & -V_1 Y_{13} \cos(\theta_1 - \theta_3 - \beta_{13}) \\ V_1 V_3 Y_{13} \cos(\theta_1 - \theta_3 - \beta_{13}) & -V_1 Y_{13} \sin(\theta_1 - \theta_3 - \beta_{13}) \end{bmatrix}$$

$$D_{SG4_{21}} = D_{SG4_{12}}$$

$$D_{SG4_{22}} = \begin{bmatrix} A_{SG4_2} & B_{SG4_2} \\ xC_{SG4_2} & D_{SG4_2} \end{bmatrix}, \text{ with}$$

$$A_{SG4_2} = -I_{d_2} V_2 \cos(\delta_2 - \theta_2) + I_{q_2} V_2 \sin(\delta_2 - \theta_2) + V_2 \sum_{k=2}^3 V_k Y_{2k} \sin(\theta_2 - \theta_k - \beta_{2k})$$

$$B_{SG4_2} = I_{d_2} \sin(\delta_2 - \theta_2) + I_{q_2} \cos(\delta_2 - \theta_2) - \sum_{k=2}^3 V_k Y_{2k} \sin(\theta_2 - \theta_k - \beta_{2k}) - V_2 Y_{2k} \cos(\theta_2 - \theta_k - \beta_{2k}) + \frac{\partial P_{L_2}(V_2)}{\partial V_2}$$

$$C_{SG4_2} = -I_{d_2} V_2 \sin(\delta_2 - \theta_2) + I_{q_2} V_2 \cos(\delta_2 - \theta_2) - V_2 \sum_{k=2}^3 V_k Y_{2k} \cos(\theta_2 - \theta_k - \beta_{2k})$$

$$D_{SG4_2} = I_{d_2} \cos(\delta_2 - \theta_2) - I_{q_2} \sin(\delta_2 - \theta_2) - \sum_{k=2}^3 V_k Y_{2k} \sin(\theta_2 - \theta_k - \beta_{2k}) - V_2 Y_{2k} \sin(\theta_2 - \theta_k - \beta_{2k}) + \frac{\partial Q_{L_2}(V_2)}{\partial V_2}$$

$$D_{SG4_{23}} = \begin{bmatrix} -V_2 V_3 Y_{23} \sin(\theta_2 - \theta_3 - \beta_{23}) & -V_2 Y_{23} \cos(\theta_2 - \theta_3 - \beta_{23}) \\ V_2 V_3 Y_{23} \cos(\theta_2 - \theta_3 - \beta_{23}) & -V_2 Y_{23} \sin(\theta_2 - \theta_3 - \beta_{23}) \end{bmatrix}$$

$$D_{SG4_{31}} = D_{SG4_{13}}$$

$$D_{SG4_{32}} = D_{SG4_{23}}$$

$$D_{SG4_{33}} = \begin{bmatrix} A_{SG4_3} & B_{SG4_3} \\ C_{SG4_3} & D_{SG4_3} \end{bmatrix}, \text{ with}$$

$$\begin{aligned}
 A_{SG4_3} &= -I_{d_3} V_3 \cos(\delta_3 - \theta_3) + I_{q_3} V_3 \sin(\delta_3 - \theta_3) + V_3 V_3 Y_{33} \sin(\theta_2 - \theta_3 - \beta_{33}) \\
 B_{SG4_3} &= I_{d_3} \sin(\delta_3 - \theta_3) + I_{q_3} \cos(\delta_3 - \theta_3) - V_3 Y_{33} \sin(\theta_3 - \theta_3 - \beta_{33}) - V_3 Y_{33} \cos(\theta_3 - \theta_3 - \beta_{33}) + \frac{\partial P_{L_3}(V_3)}{\partial V_3} \\
 C_{SG4_3} &= -I_{d_3} V_3 \sin(\delta_3 - \theta_3) + I_{q_3} V_3 \cos(\delta_3 - \theta_3) - V_3 V_3 Y_{33} \cos(\theta_3 - \theta_3 - \beta_{33}) \\
 D_{SG4_3} &= I_{d_3} \cos(\delta_3 - \theta_3) - I_{q_3} \sin(\delta_3 - \theta_3) - V_3 Y_{33} \sin(\theta_3 - \theta_3 - \beta_{33}) - V_3 Y_{33} \cos(\theta_3 - \theta_3 - \beta_{33}) + \frac{\partial Q_{L_3}(V_3)}{\partial V_3}
 \end{aligned}$$

$$\begin{aligned}
 D_{NET1} &= \begin{bmatrix} D_{NET1_{14}} & D_{NET1_{15}} & \cdots & D_{NET1_{1k}} \\ \vdots & \vdots & \dots & \vdots \\ D_{NET1_{i4}} & \cdots & \cdots & D_{NET1_{ik}} \end{bmatrix}_{6 \times 18}, \text{ with} \\
 D_{NET1_{ik}} &= \begin{bmatrix} -V_i V_k Y_{ik} \sin(\theta_i - \theta_k - \beta_{ik}) & -V_i Y_{ik} \cos(\theta_i - \theta_k - \beta_{ik}) \\ V_i V_k Y_{ik} \cos(\theta_i - \theta_k - \beta_{ik}) & -V_i Y_{ik} \sin(\theta_i - \theta_k - \beta_{ik}) \end{bmatrix}
 \end{aligned}$$

The state-space model of the load buses is given by Equation (42). It is obtained by linearising Equations (39) and (40) around the operating point and by neglecting all the second-order terms associated with the small variations. In addition, $\partial P_{L_i}(V_i)/\partial V_i$ and $\partial Q_{L_i}(V_i)/\partial V_i$ are assumed to be zero because conventional loads are considered to be constant power loads.

$$0 = D_{SG5} \Delta V_g + D_{NET2} \Delta V_{NET} \tag{42}$$

Matrices D_{SG5} and D_{NET2} are given by:

$$\begin{aligned}
 D_{SG5} &= \begin{bmatrix} D_{SG5_{41}} & \cdots & D_{SG5_{4i}} \\ \vdots & \vdots & \vdots \\ D_{SG5_{k1}} & \cdots & D_{SG5_{ki}} \end{bmatrix}_{18 \times 6}, \text{ with} \\
 D_{SG5_{ki}} &= \begin{bmatrix} -V_i V_k Y_{ik} \sin(\theta_i - \theta_k - \beta_{ik}) & V_i Y_{ik} \cos(\theta_i - \theta_k - \beta_{ik}) \\ -V_i V_k Y_{ik} \cos(\theta_i - \theta_k - \beta_{ik}) & V_i Y_{ik} \sin(\theta_i - \theta_k - \beta_{ik}) \end{bmatrix}
 \end{aligned}$$

$$\begin{aligned}
 D_{NET2} &= \begin{bmatrix} D_{NET2_{44}} & \cdots & D_{NET2_{4k}} \\ \vdots & \vdots & \vdots \\ D_{NET2_{i4}} & \cdots & D_{NET2_{ik}} \end{bmatrix}_{18 \times 18}, \text{ with} \\
 D_{NET2_{ik \neq k}} &= \begin{bmatrix} -V_i V_k Y_{ik} \sin(\theta_i - \theta_k - \beta_{ik}) & -V_i Y_{ik} \cos(\theta_i - \theta_k - \beta_{ik}) \\ V_i V_k Y_{ik} \cos(\theta_i - \theta_k - \beta_{ik}) & -V_i Y_{ik} \sin(\theta_i - \theta_k - \beta_{ik}) \end{bmatrix}
 \end{aligned}$$

$$D_{NET2_{ik=k}} = \begin{bmatrix} \sum_{k=4}^{12} V_i V_k Y_{ik} \sin(\theta_i - \theta_k - \beta_{ik}) & \frac{\partial P_{L_i}(V_i)}{\partial V_i} - \sum_{k=4}^{12} V_k Y_{ik} \cos(\theta_i - \theta_k - \beta_{ik}) - V_i Y_{ik} \cos(\theta_i - \theta_k - \beta_{ik}) \\ -\sum_{k=4}^{12} V_i V_k Y_{ik} \cos(\theta_i - \theta_k - \beta_{ik}) & \frac{\partial Q_{L_i}(V_i)}{\partial V_i} - \sum_{k=4}^{12} V_k Y_{ik} \sin(\theta_i - \theta_k - \beta_{ik}) - V_i Y_{ik} \sin(\theta_i - \theta_k - \beta_{ik}) \end{bmatrix}$$

In D_{SG3_i} , $D_{NET1_{ik}}$, and $D_{SG5_{ki}}$, i and k represent the generator buses ($i = 1, 2,$ and 3) and the non-generator buses ($k = 4$ to 12), respectively, whereas in $D_{NET2_{ik \neq k}}$ and $D_{NET2_{ik=k}}$, i and k are the load buses ($i = 4$ to 12) and the non-generator buses ($k = 4$ to 12), respectively.

3.4. Complete Small-Signal State-Space Model of the Test System

The complete state-space model of the test system (Figure 1) is represented by Equations (43)–(46). It is obtained from the developed individual submodels given by Equations (27)–(29), (34), (41), and (42).

$$\Delta \dot{X}_{SGEL} = A_{SGEL} \Delta X_{SGEL} + B_{SG1} \Delta I_g + B_{SG2} \Delta V_g + B_{SGEL} \Delta U_{SGEL} \tag{43}$$

$$0 = C_{SGEL1} \Delta X_{SGEL} + D_{SG1} \Delta I_g + D_{SG2} \Delta V_g \tag{44}$$

$$0 = C_{SGEL2} \Delta X_{SGEL} + D_{SG3} \Delta I_g + D_{SG4} \Delta V_g + D_{NET1} \Delta V_{NET} \tag{45}$$

$$0 = D_{SG5}\Delta V_g + D_{NET2}\Delta V_{NET} \tag{46}$$

with $A_{SGEL} = \begin{bmatrix} A_{SG} & 0 \\ 0 & A_{EL} \end{bmatrix}_{16 \times 16}$; $\Delta X_{SGEL} = [\Delta X^T \ \Delta i_{dc}]^T_{16 \times 1}$; $B_{SGEL} = \begin{bmatrix} B_{SG3} & 0 \\ 0 & B_{EL} \end{bmatrix}_{16 \times 7}$;
 $\Delta U_{SGEL} = [\Delta U^T \ \Delta \alpha]^T_{7 \times 1}$; $C_{SGEL1} = \begin{bmatrix} C_{SG1} & 0 \\ 0 & 0 \end{bmatrix}_{7 \times 16}$ and $C_{SGEL2} = C_{SGEL}$.

By eliminating ΔI_g from Equations (43)–(46), the complete model is rewritten as:

$$\begin{bmatrix} \Delta \dot{X} \\ 0 \\ 0 \end{bmatrix} = \begin{bmatrix} A_{SGEL} - B_{SG1}D_{SG1}^{-1}C_{SGEL1} & B_{SG2} - B_{SG1}D_{SG1}^{-1}D_{SG2} & 0 \\ C_{SGEL2} - D_{SG3}D_{SG1}^{-1}C_{SGEL1} & D_{SG4} - D_{SG3}D_{SG1}^{-1}D_{SG2} & D_{NET1} \\ 0 & D_{SG5} & D_{NET1} \end{bmatrix} \begin{bmatrix} \Delta X_{SGEL} \\ \Delta V_g \\ \Delta V_{NET} \end{bmatrix} + \begin{bmatrix} B_{SGEL} \\ 0 \\ 0 \end{bmatrix} \Delta U_{SGEL} \tag{47}$$

According to Equation (47), the complete state-space model of the test system can be expressed as:

$$\Delta \dot{X} = A_{grid}\Delta X + B_{grid}\Delta U \tag{48}$$

where A_{grid} is the dynamic matrix of the grid, and B_{grid} represents the input matrix. The effect of the PEM electrolyser on the small-signal angular stability is examined through the movement of the eigenvalues from the dynamic matrix in the complex plane. The complete form of the dynamic matrix is expressed by:

$$[A_{grid}] = [A_{SGEL} - B_{SG1}D_{SG1}^{-1}C_{SGEL1}] - [B_{SG2} - B_{SG1}D_{SG1}^{-1}D_{SG2} \ 0] \begin{bmatrix} D_{SG4} - D_{SG3}D_{SG1}^{-1}D_{SG2} & D_{NET1} \\ D_{SG5} & D_{NET1} \end{bmatrix}^{-1} \begin{bmatrix} C_{SGEL2} - D_{SG3}D_{SG1}^{-1}C_{SGEL1} \\ 0 \end{bmatrix}$$

4. Stability Analysis Results

The impact of 100 MW of PEM electrolysers on the stability of the small-signal rotor angle was assessed by analyzing the state-space models associated with the synchronous generators, the PEM electrolyser, and the network as described in the test system (Figure 1). The calculation of the test system’s eigenvalues was performed using Matlab. The obtained results were then verified through time-domain simulations. Table 2 lists the parameter values of the synchronous generators and of the static exciters.

Table 2. Parameter values for test-system components.

Machine 1	Machine 2	Machine 3
$P_{G1} = 270$ MW	$P_{G2} = 150$ MW	$P_{G3} = 410$ MW
$Q_{G1} = 81$ MVar	$Q_{G2} = 45$ MVar	$Q_{G3} = 123$ MVar
$R_{s1} = 0.089$ pu, $X_{d1} = 1.5$ pu	$R_{s2} = 0.089$ pu, $X_{d2} = 1.5$ pu	$R_{s3} = 0.089$ pu, $X_{d3} = 1.5$ pu
$X'_{d1} = 0.18$ pu, $T'_{d1} = 5$ s	$X'_{d2} = 0.18$ pu, $T'_{d2} = 5$ s	$X'_{d3} = 0.18$ pu, $T'_{d3} = 6$ s
$X'_{q1} = 1.26$ pu, $T'_{q1} = 0.31$ s	$X'_{q2} = 1.26$ pu, $T'_{q2} = 0.31$ s	$X'_{q3} = 1.26$ pu, $T'_{q3} = 0.53$ s
$X_{q1} = 1.26$ pu, $H_1 = 3.4$ s	$X_{q2} = 1.26$ pu, $H_2 = 2.6$ s	$X_{q3} = 1.26$ pu, $H_3 = 3.7$ s
$D_1 = 0.5$	$D_2 = 0.5$	$D_3 = 0.6$
Static exciter 1	Static exciter 2	Static exciter 3
$K_{A1} = 20$, $T_{A1} = 0.02$ s	$K_{A2} = 20$, $T_{A2} = 0.02$ s	$K_{A3} = 20$, $T_{A3} = 0.02$ s
$K_{F1} = 0.063$, $T_{F1} = 0.35$ s	$K_{F1} = 0.063$, $T_{F2} = 0.35$ s	$K_{F1} = 0.063$, $T_{F3} = 0.35$ s
$K_{E1} = 1$, $T_{E1} = 0.314$ s	$K_{E2} = 1$, $T_{E1} = 0.314$ s	$K_{E3} = 1$, $T_{E1} = 0.314$ s

4.1. Dominant Modes in Steady State

4.1.1. Without Connecting the PEM Electrolyser to the Test System

Figure 12a shows the modelling results obtained without connecting the PEM electrolyser to Busbar 4. The obtained dominant modes of synchronous generators coupled with the test system under steady-state conditions are located in the left half-complex plane. The obtained dominant modes are described in Table 3. Fifteen modes were clearly identified. Conjugate complexes $\lambda_{1,2}$, $\lambda_{3,4}$, and $\lambda_{5,6}$ are identified in Table 3. λ_1 and λ_2

are the electromechanical modes associated with the rotor angle deviation ($\Delta\delta_1$) and rotor speed deviation ($\Delta\omega_1$) of SG 1. λ_3 and λ_4 are the electromechanical modes coupled with SG 2, and λ_5 and λ_6 are the electromechanical modes related to SG 3.

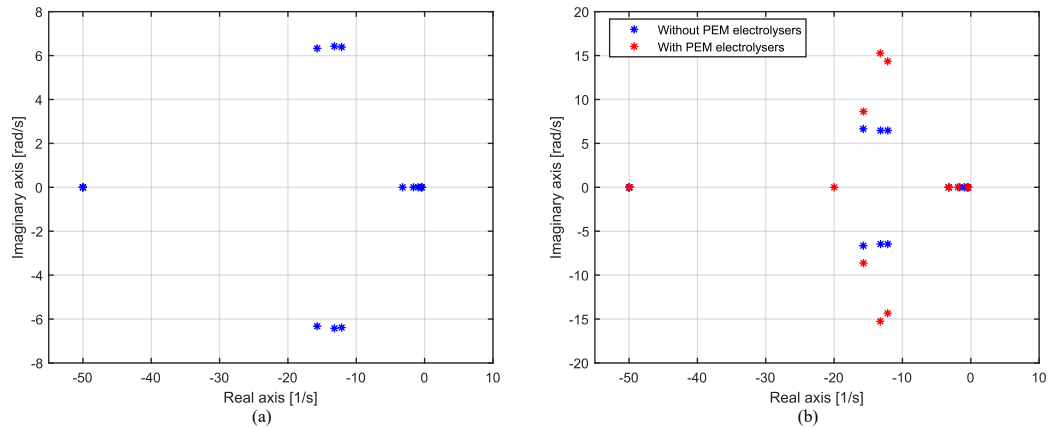


Figure 12. The modelled system’s modes in the complex plane: (a) without connecting the PEM electrolyser to test system; (b) with 100 MW of PEM electrolyzers connected to the grid. The modes in the absence of the electrolyzer are depicted in blue, while those incorporating the electrolyzer are illustrated in red.

One can note that the oscillation frequency of these electromechanical modes is close to 1 Hz (63,862 rad/s). This illustrates that the interconnected synchronous machines maintain their synchronism around 50 Hz after being subjected to a small disturbance. The values of these modes are close because the used parameter values of the synchronous generators are close (see Table 2). The effects of the PEM electrolyser on the angular stability must be investigated with respect to these modes.

Modes λ_{13} , λ_{14} , and λ_{15} are associated with the field voltage variations (ΔE_{fd_i}) of static exciters. Modes λ_{10} , λ_{11} , and λ_{12} are related to the magnetic flux variations of damper winding (ΔE_{d_i}) of synchronous machines, whereas modes λ_7 , λ_8 , and λ_9 are coupled with the magnetic flux variations of field winding (ΔE_{q_i}) of synchronous machines. Figure 12a and Table 3 show that the modes associated with ΔE_{fd_i} are identical to the three exciters using the same parameter values.

Table 3. Identification of modes with respect to the state variables of synchronous generators in the case in which the PEM electrolyser is not connected to the test system.

Mode Values	Identification of Modes
$\lambda_1, \lambda_2: -12.1368 \pm j6.3862$	$\Delta\delta_1$ and $\Delta\omega_1$
$\lambda_3, \lambda_4: -15.7177 \pm j6.3269$	$\Delta\delta_2$ and $\Delta\omega_2$
$\lambda_5, \lambda_6: -13.1985 \pm j6.4232$	$\Delta\delta_3$ and $\Delta\omega_3$
$\lambda_7, \lambda_8, \lambda_9: -1.6326, -0.9495$ and -0.4654	$\Delta E'_{q_1}, \Delta E'_{q_2}$ and $\Delta E'_{q_3}$
$\lambda_{10}, \lambda_{11}, \lambda_{12}: -0.5125, -0.3880, -0.4654$	$\Delta E'_{d_1}, \Delta E'_{d_2}$ and $\Delta E'_{d_3}$
$\lambda_{13}, \lambda_{14}, \lambda_{15}: -49.9982, -49.9928, -49.9992$	$\Delta E_{fd_1}, \Delta E_{fd_2}$ and ΔE_{fd_3}

4.1.2. With the PEM Electrolyser Connected to the Test System

Figure 12b shows the modelling results obtained when 100 MW of PEM electrolyzers were connected to Busbar 4. The results show that the electrolyser model adds an additional negative real mode ($\lambda_{16} = -19.9835$). This mode is associated with the DC electrolyser current variation (Δi_{dc}). In addition, the modes related to the static exciters and the magnetic flux of field winding and the damper winding are not significantly influenced by the PEM electrolyser, as shown in Figure 12b and in Table 4. This is because the dynamic response of the electrolyser current is more related to the voltage angle of the system than to the voltage amplitude. For this reason, the damping and oscillation frequency of the

electromechanical modes ($\lambda_{1,2}$, $\lambda_{3,4}$, and $\lambda_{5,6}$) are significantly affected. In terms of the damping of the electromechanical modes, the effect of the PEM electrolyser is less profound than for the oscillation frequency of these modes. As observed in Figure 12b, there is a large increase in the oscillation frequency of the electromechanical conjugate modes associated with SG 1 ($\lambda_{1,2}$) and SG 3 ($\lambda_{5,6}$) than in the electromechanical modes of SG 2 ($\lambda_{3,4}$). This is caused by the electrical distance between the generator buses and the electrolyser bus. On the other hand, the PEM electrolyser increases the damping of the electromechanical modes associated with the synchronous machine connected to the same busbar ($\lambda_{1,2}$).

Table 4. Identification of modes with respect to the state variables of synchronous generators in the case in which 100 MW of PEM electrolysers are connected to the test system (*Busbar 4*).

Mode Values	Identification of Modes
$\lambda_1, \lambda_2: -12.1649 \pm j14.3415$	$\Delta\delta_1$ and $\Delta\omega_1$
$\lambda_3, \lambda_4: -15.6977 \pm j8.6270$	$\Delta\delta_2$ and $\Delta\omega_2$
$\lambda_5, \lambda_6: -13.2407 \pm j15.2628$	$\Delta\delta_3$ and $\Delta\omega_3$
$\lambda_7, \lambda_8, \lambda_9: -3.2258, -3.2258$ and -1.8868	$\Delta E'_{q1}, \Delta E'_{q2}$ and $\Delta E'_{q3}$
$\lambda_{10}, \lambda_{11}, \lambda_{12}: -0.4113, -0.4836, -0.3505$	$\Delta E'_{d1}, \Delta E'_{d2}$ and $\Delta E'_{d3}$
$\lambda_{13}, \lambda_{14}, \lambda_{15}: -49.9760, -49.9431, -49.9873$	$\Delta E_{fd1}, \Delta E_{fd2}$ and ΔE_{fd3}
$\lambda_{16}: -19.9835$	Δi_{dc}

4.1.3. Impact of the Synchronous Generator Parameters on the Movement of Electromechanical Modes

- Impact of the inertial constant:

Figures 13–15 show the impact of a change in the inertial constant on the trajectories of the electromechanical modes. With respect to changes in the inertial constant (H_1) from 3 s to 7 s, Figure 13 shows that larger values of H_1 decrease the damping and the oscillation frequency of the system modes (λ_1 and λ_2) associated with SG 1. On the other hand, the modes related to SG 2 and SG 3 are not affected by this variation. This shows that the choice of H_1 values becomes a critical factor in the dynamic response of the machine if the electrolyser is connected to the same busbar with the synchronous generator. Note that to reach the initial oscillation frequency (≈ 1 Hz), the inertial constant has to be increased but at the risk of reducing the stability margin.

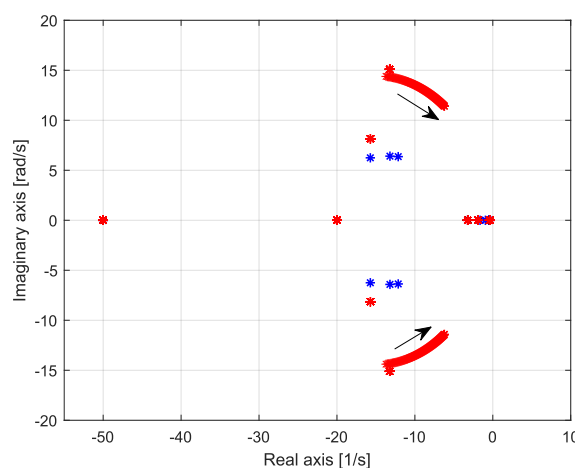


Figure 13. Movement of modes λ_1 and λ_2 caused by changes in the inertial constant value of the synchronous generator connected to *Busbar 4*: $H_1 = 3$ to 7 s. The modes in the absence of the electrolyzer are depicted in blue, while those incorporating the electrolyzer are illustrated in red.

Figure 14 depicts the movement of modes λ_3 and λ_4 caused by changes in the inertial constant (H_2) from 2.6 s to 7 s. As in the previous case, only the electromechanical modes of SG 2 are affected. The oscillation frequencies of these modes are less affected than

those of SG 1 and SG 3. However, it is observed that the larger values of H_2 decrease the damping of the modes. On the other hand, larger values of H_2 have no significant impact on the oscillation frequency of the λ_3 and λ_4 modes. This can be attributed to the electrical distance between *Busbar 6* of SG 2 and *Busbar 4* of the electrolyser. The capacity of this synchronous machine can also have an influence on the observed trajectories of the modes.

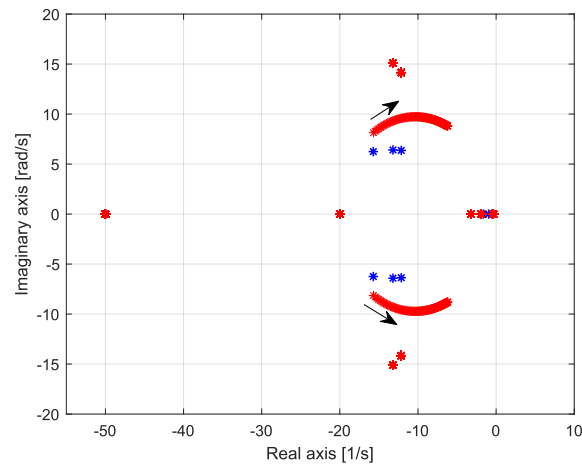


Figure 14. Movement of- the λ_3 and λ_4 modes caused by changes in the inertial constant value of the synchronous generator connected to *Busbar 6*: $H_2 = 2.6$ to 7 s. The modes in the absence of the electrolyzer are depicted in blue, while those incorporating the electrolyzer are illustrated in red.

Finally, Figure 15 shows the impact of changes in the inertial (constant) H_3 on the trajectories of the λ_5 and λ_6 modes. Note that the oscillation frequencies of these modes decrease with an increase in H_3 , and larger values of H_3 lead to decreases in the damping of these modes. As in the previous cases, to reach the initial oscillation frequency (≈ 1 Hz), the inertial constant must be increased, but the technical limits cannot be exceeded.

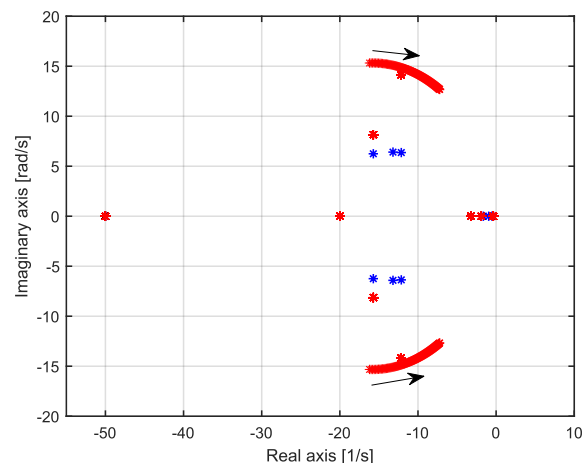


Figure 15. Movement of the λ_5 and λ_6 modes caused by changes in the inertial constant value of the synchronous generator connected to *Busbar 11*: $H_3 = 3$ to 7 s. The modes in the absence of the electrolyzer are depicted in blue, while those incorporating the electrolyzer are illustrated in red.

- Impact of the damping torque coefficient

The impacts of the damping torque coefficient on the movement of the electromechanical modes are illustrated from Figures 16–18. These results indicate that the damping torque coefficient has a significant impact on the damping and oscillation frequency of the electromechanical modes. Figure 16 reveals that the oscillation frequencies of the λ_1 and λ_2 modes decrease with increases in the value of the damping torque coefficient (D_1) SG 1. In contrast, the damping of these modes is increased. The effect of this coefficient

on the modes is opposite to that of the inertial constant in terms of oscillation frequency and damping of the electromechanical modes. As observed in Figure 16, the oscillation frequency of the affected modes can return to the initial condition value (≈ 1 Hz).

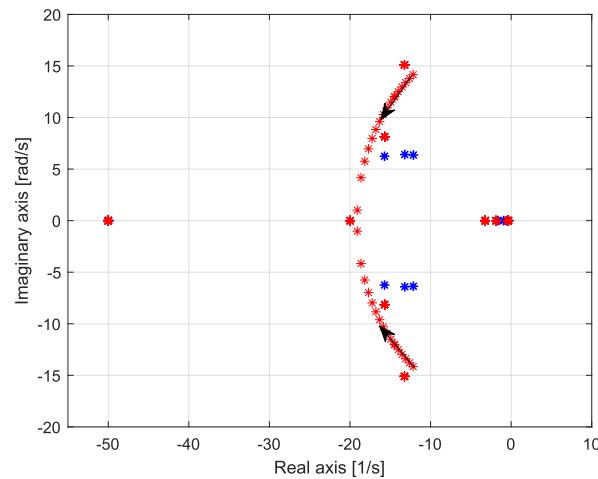


Figure 16. Movement of the λ_1 and λ_2 modes caused by changes in the damping torque coefficient value of the synchronous generator connected to *Busbar 4*: $D_1 = 0.5$ to 0.8 . The modes in the absence of the electrolyzer are depicted in blue, while those incorporating the electrolyzer are illustrated in red.

Figure 17 shows that higher values of the damping torque coefficient (D_2) of *SG 2* have a significant impact on the oscillation frequency of the λ_3 and λ_4 modes. These oscillation frequencies reach zero for certain values of D_2 . Note that the damping of the λ_3 mode increases when that of the λ_4 mode decreases. The observed trajectories of the λ_3 and λ_4 modes may be due to their small capacity compared to that of the other two generators. The electrical distance between *SG 2* and the electrolyser can also be a cause of this phenomenon.

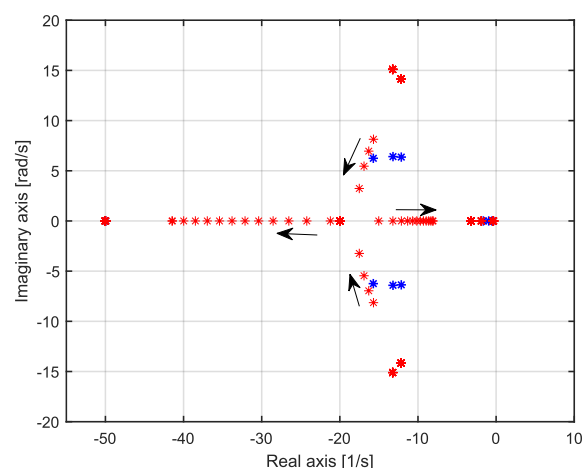


Figure 17. Movement of the λ_3 and λ_4 modes caused by changes in the damping torque coefficient value of the synchronous generator connected to *Busbar 4*: $D_2 = 0.5$ to 0.8 . The modes in the absence of the electrolyzer are depicted in blue, while those incorporating the electrolyzer are illustrated in red.

Figure 18 shows the effect of increasing the value of D_3 associated with *SG 3* on the λ_5 and λ_6 modes. These results are close to those obtained for *SG 1* (Figure 16). Note that the oscillation frequency of modes decreases with an increasing damping torque coefficient. The trajectories of the two groups of modes are different. These trajectories illustrate that the modes coupled to *SG 1* are more affected than those associated with *SG 2* and *SG 3*.

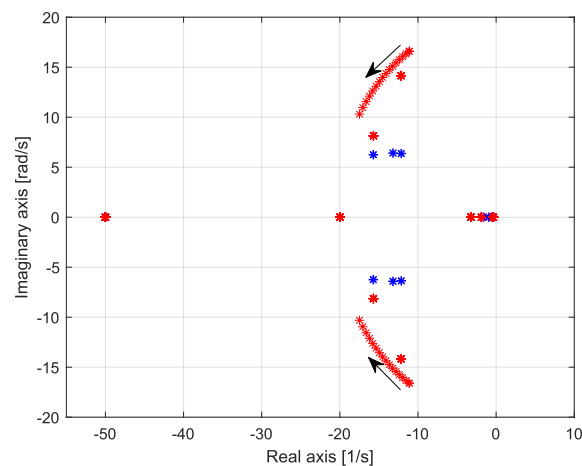


Figure 18. Movement of the λ_5 and λ_6 modes caused by changes in the damping torque coefficient value of a synchronous generator connected to *Busbar 4*: $D_3 = 0.5$ to 0.8 . The modes in the absence of the electrolyzer are depicted in blue, while those incorporating the electrolyzer are illustrated in red.

4.2. Time-Domain Simulations

The obtained eigenvalue analysis results were consolidated through time-domain simulations implemented in the Matlab/Simulink/Simscape environment. The test power system depicted in Figure 1 was implemented with the same parameter values as those listed in Table 2. Two small disturbances were considered. The first one is the connection of the 100 MW of PEM electrolyzers to the test system. The second disturbance consists of a decrease in the electrolyser current set point of 1%, from 21.794 kA to 21.576 kA. The dynamic response of the rotor angle deviation and rotor speed deviation were investigated to examine the small-signal angular stability. The impact of the proposed electrolyser model as a load on the rotor-angle stability was also examined.

Dynamic Response of Electromechanical State Variables

- Connecting the electrolyser to the test system:

The first scenario consists of connecting the 100 MW of PEM electrolyzers to *Busbar 4* at $t = 15$ s. The obtained results are illustrated in Figures 19–22. It is observed that the interconnected synchronous machines maintain synchronism. This is shown by the rotor speed deviations ($\Delta\omega_1$, $\Delta\omega_2$, and $\Delta\omega_3$) of SG 1, SG 2, and SG 3, which are zero before and after connecting the electrolyser (Figure 19a). Figure 19 also illustrates the influence of the line impedance between the electrolyser busbar and the synchronous generator busbars. For example, the dynamic response of the rotor speed deviation ($\Delta\delta_1$) of SG 1 is different than that of $\Delta\delta_2$ and $\Delta\delta_3$, as shown in Figure 19a. Because SG 1 is connected to *Busbar 4*, the connection of the 100 MW of PEM electrolyzers to *Busbar 4* is perceived by SG 1 as an increase in electrical power in an attempt to reduce the frequency and, therefore, the rotor angle deviation. It is observed that the connection of the electrolyser is regarded by SG 2 and SG 3 as an increase in frequency and, therefore, an increase in the rotor angle deviation. Note that the variation of SG 1 is higher than that of SG 2 and SG 3. In contrast, the settling time for SG 1 is shorter than for SG 2 and SG 3. Figure 19b shows that the PEM improves the oscillation magnitudes of the rotor speed deviation of the synchronous machine connected to the same busbar. The oscillation amplitudes of SG 1 are smaller than those of SG 2 and SG 3. The electrolyser provides a damping effect on the synchronous machine connected to the same busbar.

The influence of the proposed model of the electrolyser as a load is also shown in Figures 20–22. Three ways of connecting PEM electrolyzers were considered, as described in Figure 9. The first consists of using two electrochemical submodels, i.e., 2×50 MW in parallel on the DC side of the 12-pulse thyristor rectifier. The second is to use four electrochemical submodels in parallel, i.e., 4×25 MW. The last one is to use one electrochemical

model, i.e., 1×100 MW. These three ways affect the dynamic response of the rotor angle deviation and of the rotor speed deviation, as illustrated in Figures 20–22. Note that the dynamic responses associated with the 2×50 MW and 4×25 MW cases are close. This is due to the electrolyser being seen by the system as a dominant constant current load. Figures 20b, 21b, and 22b show that the 2×50 MW connection mode allows the PEM electrolyser to act as constant current loads. This supports the modelling result presented in Section 2.3.

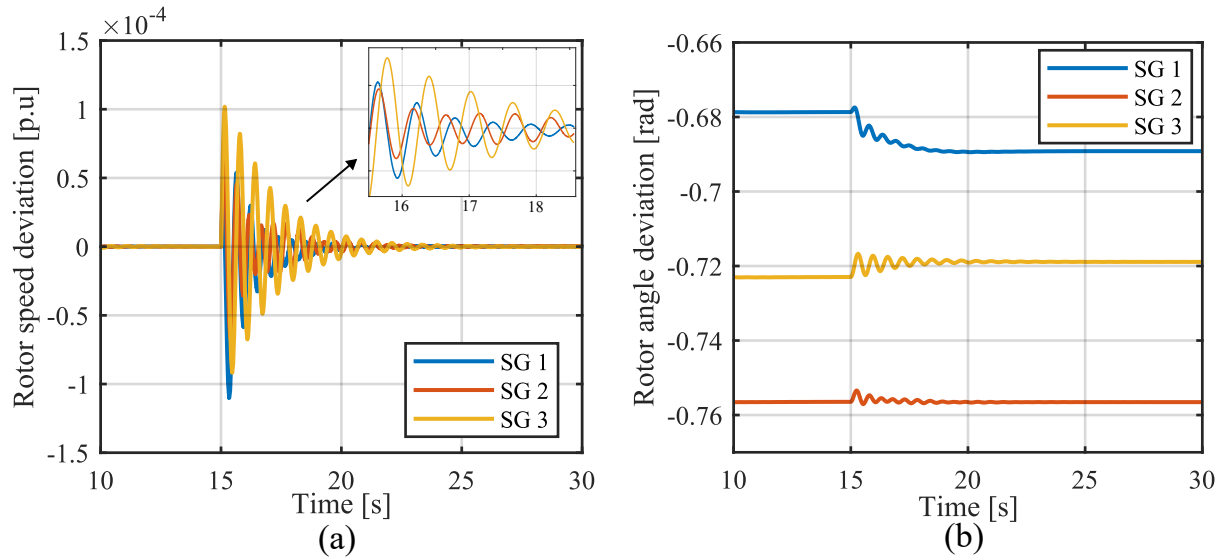


Figure 19. (a) Dynamic response of the rotor speed deviations ($\Delta\omega_i$) and (b) the dynamic response of the rotor angle deviations ($\Delta\theta_i$).

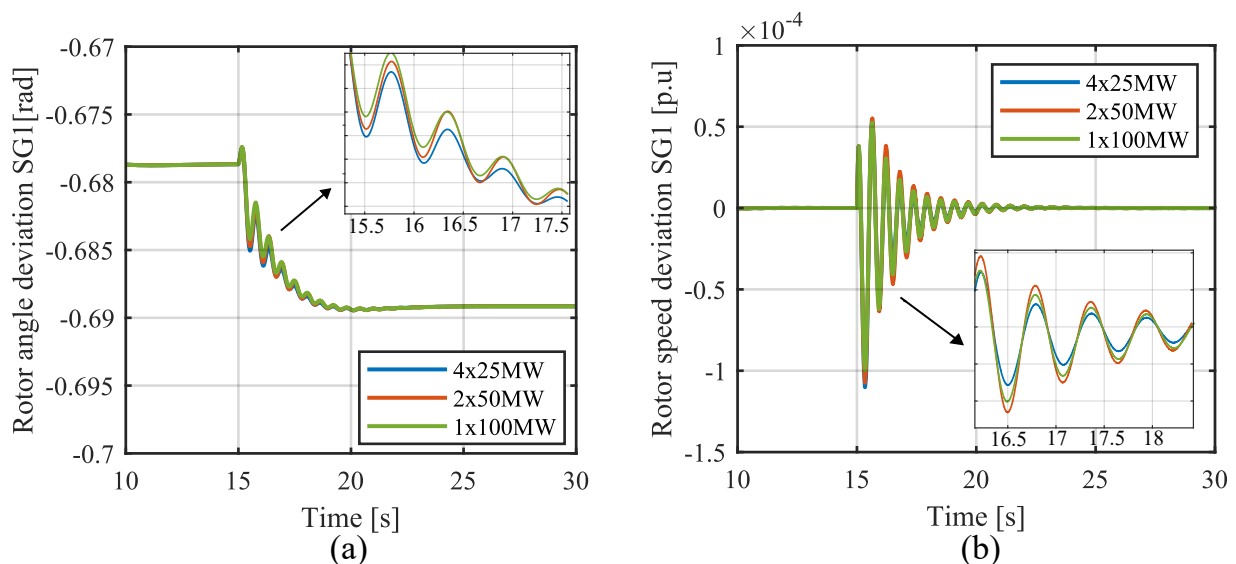


Figure 20. Dynamic response of electromechanical state variables of SG 1 when 100 MW of PEM electrolyser are connected to the grid at 15 s: (a) rotor angle deviation and (b) rotor speed deviation with the impact of modelling the electrolyser as a load.

The obtained results show that the effect of modelling the electrolyser as a load is more significant on the rotor angle variation and the rotor speed variation of the generator that shares the same busbar with the electrolyser.

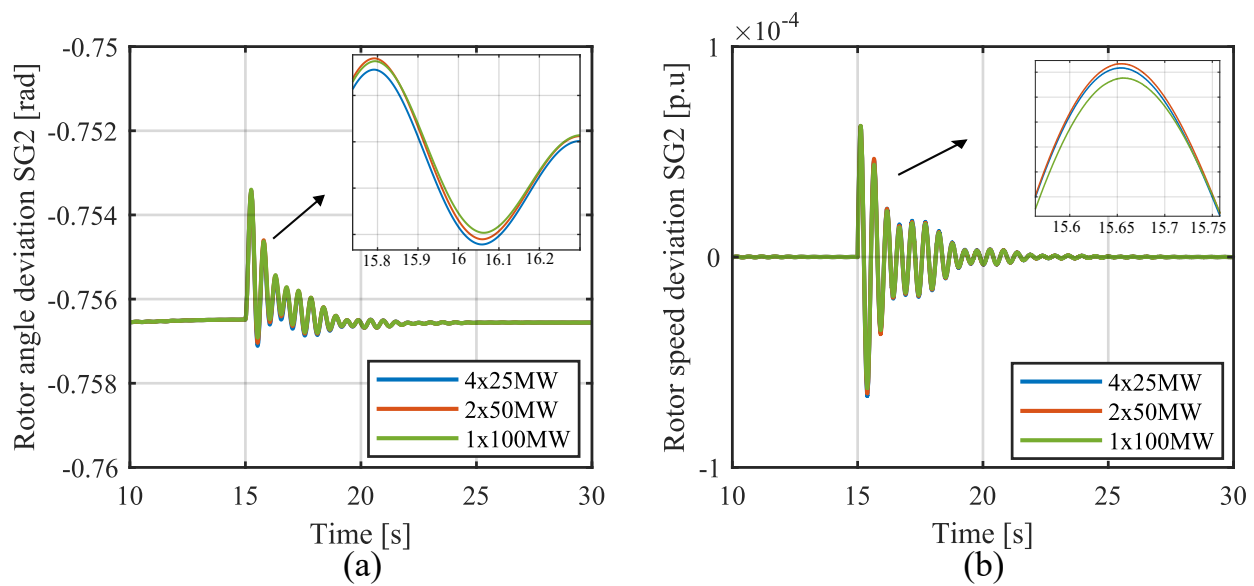


Figure 21. Dynamic response of electromechanical state variables of SG 2 when 100 MW of PEM electrolyzers are connected to the grid at 15 s: (a) rotor angle deviation and (b) rotor speed deviation with the impact of modelling the electrolyser as a load.

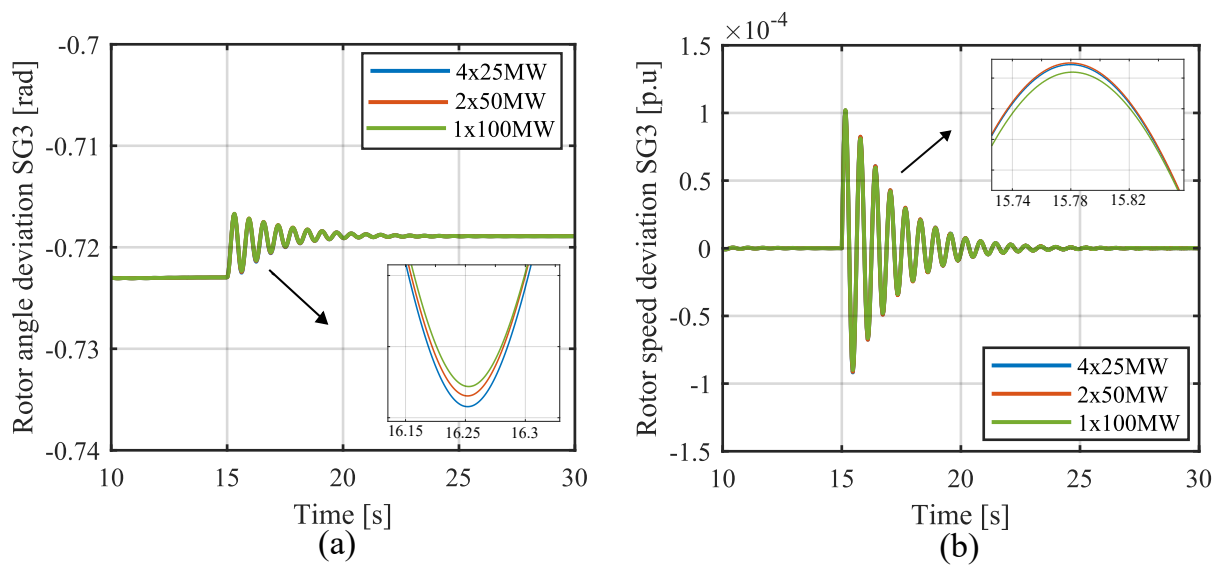


Figure 22. Dynamic response of electromechanical state variables of SG 3 when 100 MW of PEM electrolyzers are connected to the grid at 15 s: (a) rotor angle deviation and (b) rotor speed deviation with the impact of modelling the electrolyser as a load.

- Decrease in the electrolyser current set point:

Figure 23 shows the results obtained by changing the electrolyser current set point from 21.797 kA to 21.577 kA (i.e., a 1% reduction). Figure 23a illustrates that the proposed current controller maintains the electrolyser current at the desired value. Figure 23b shows that the synchronism of the interconnected synchronous machines is maintained. The observed settling time is close to that of the first scenario.

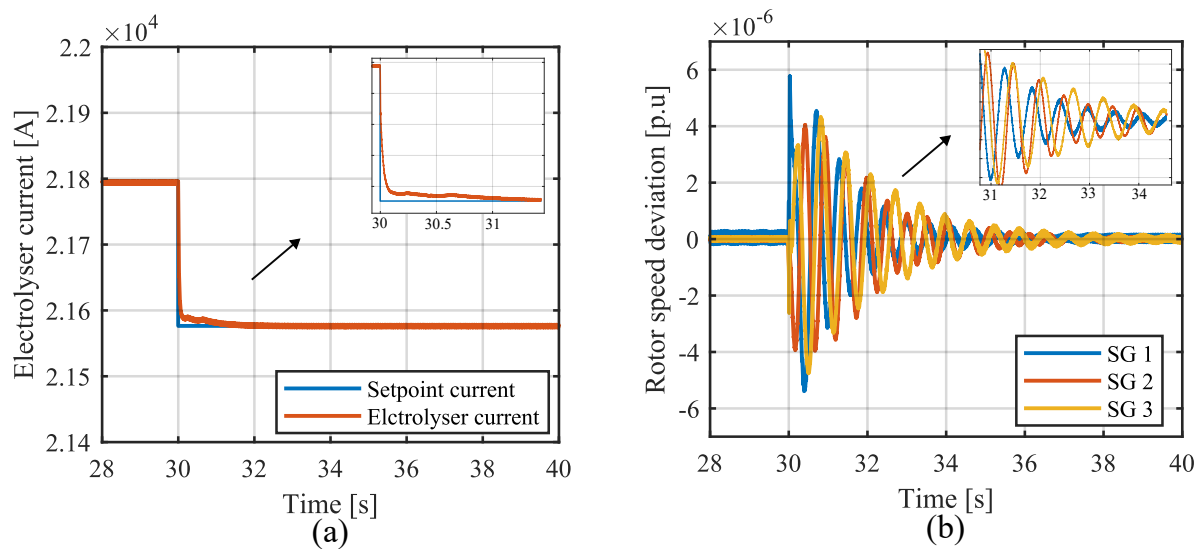


Figure 23. Dynamic responses of electromechanical state variables of $SG i$ of electrolyser current: (a) DC electrolyser current and (b) rotor speed deviations $\Delta\omega_i$.

5. Conclusions

The effect of a large PEM electrolyser on the small-disturbance rotor angle stability was analyzed in this paper. First, the dynamic modelling of the PEM electrolyser and the control structure of the electrolyser current was proposed. Since several electrochemical PEM electrolyser models have been proposed in the literature, in this paper, we proposed a comparative analysis of the cell voltage dynamic response of these models to identify which model presents a better dynamic response. The time constant was considered as the metric for comparison and selection. The dynamic model of the selected PEM electrolyser was then used to propose a control structure to adjust the electrolyser current via the firing angle of a 12-pulse thyristor rectifier. Afterwards, we showed that as a load, the PEM electrolyser can be modelled as a combination of a constant impedance load fraction and a constant current load fraction. We showed that the percentage of the load modelled as either a constant impedance or a constant current load depends on the connection of the PEM electrolyser model to the DC side of the 12-pulse thyristor rectifier. Finally, the influence of the electrolyser on the rotor angle stability was assessed using an analytical analysis and time-domain simulations. The first method used a state-space model to evaluate the trajectories of the eigenvalues in the left-half complex plane. The obtained results show that the PEM electrolyser affects the electromechanical modes of synchronous machines. This effect consists of an increase in the oscillation frequencies of the modes and a decrease in the damping of the electromechanical modes. In contrast, it increases the damping of the electromechanical modes associated with the synchronous machine connected to the same busbar. The results show that to mitigate this effect, either the inertial constant or the damping torque coefficient can be adjusted. However, this can lead to a tradeoff between the two parameters when high values have to be set. The analytical results were validated through time-domain simulations. The results show the efficiency of the proposed control structure of the electrolyser current and the proposed model of the electrolyser when viewed as a load. In future work, the effect of a large PEM electrolyser on transient rotor angle stability will be addressed.

Author Contributions: Conceptualization, G.W.N., E.V.M., and E.D.J.; methodology, G.W.N., E.V.M., and E.D.J.; validation, G.W.N. and E.D.J.; investigation, G.W.N., E.V.M., and E.D.J.; writing—original draft preparation, G.W.N. and E.V.M.; writing—review and editing, G.W.N., E.V.M., and E.D.J. All authors have read and agreed to the published version of the manuscript.

Funding: This research is supported by the Energy Transition Funds project “BEST” organized by the Belgian FPS economy.

Institutional Review Board Statement: Not applicable.

Informed Consent Statement: Not applicable.

Data Availability Statement: Data are contained within the article.

Conflicts of Interest: The authors declare no conflict of interest.

Abbreviations

The following abbreviations and symbols are used in this manuscript:

PEM	Proton exchange membrane
SGs	Synchronous generators
PLL	Phase-locked loops
PI	Proportional–integral
EL	Electrolyser

Nomenclature

α	Rectifier firing angle
α_0	Nominal rectifier firing angle
a_1	Fraction of the load represented as a constant impedance load
a_2	Fraction of the load represented as a constant current load
A_{grid}	Dynamic matrix of the grid for the complete state-space model of the test system
B_{grid}	Input matrix for the complete state-space model of the test system
C_{dli}	Double layer capacity
C_{SGEL}	Observation matrix associated with the synchronous generators and electrolyser
δ_i	Relative rotor angle
ΔI_g	Vector matrix of current components of the synchronous generator
ΔU_g	Input matrix of the synchronous generator
$\Delta \theta$	Phase-angle submatrix of the network buses
ΔV	Voltage magnitude submatrix of the network buses
ΔV_g	Vector matrix of voltage magnitude and angle of the synchronous generator bus
ΔV_{NET}	Vector matrix formed by the voltage magnitude and angle submatrices of the network buses
ΔX	State vector composed of the state subvector of each synchronous generator
ΔX_{EL}	State variable of the electrolyser
ΔX_{SGEL}	State vector of generators and the electrolyser connected to the generator buses
D_i	Damping torque coefficient
D_{SGi}	Direct transmission matrices
D_{SGik}	Submatrix associated with the synchronous generator
E_{fd_i}	Field voltage
H_i	Inertial constant
i_{cell}	Input current of the cell
i_{dc}	DC current of the electrolyser
i_{dc0}	Nominal electrolyser DC current at nominal active power
k	Ratio between the secondary and primary RMS phase-to-phase voltage of the transformer
k_i	Gain of the integral controller
k_p	Gain of the proportional controller
λ_i	Modes
L_f	Filter inductance
L_{int}	Interphase inductances
L_T	Leakage inductance of the transformer
μ	Overlap angle
ψ_{1q_i}	Damper winding 1q flux linkages
P_{EI0}	Rated active power of the electrolyser
P_{EI}	Active power of the electrolyser
P_{G_i}	Active power injected into bus i
P_{L_i}	Active power of the constant power load
Q_{G_i}	Reactive power injected into bus i

Q_{L_i}	Reactive power of the constant power load
R_{ct}	Charge transfer resistance
$R_{ct,a}$	Charge transfer resistance at the anode
$R_{ct,c}$	Charge transfer resistance at the cathode
R_d	Diffusion resistance
R_i	Charge transfer resistance
R_m	Ohmic resistance during the water-splitting reaction
τ_d	Diffusion time constant
θ_i	Rotor angle
T'_{dqo_i}	Transient time constants along the d axis and q axis
T_{M_i}	Mechanical torque
U_p	RMS phase-to-phase voltage at the primary end of the transformer
U_s	RMS phase-to-phase voltage at the secondary end of the transformer
V_{act}	Activation overpotential
$V_{act,a}$	Activation overpotential at the anode
$V_{act,c}$	Activation overpotential at the cathode
V_{cell}	Cell voltage across the proton exchange membrane stack
V_{rev}	Reverse voltage potential during the water-splitting reaction
ω_i	Speed of the rotor
ω_s	Synchronous angular speed of the rotor
X_{dq}	Synchronous reactances along the d axis and q axis
X_{1q_i}	Damper winding $1q$ reactance
X_{fd_i}	Field d -axis reactance
X_{mdq_i}	Magnetizing reactances along the d axis and q axis
X'_{dq_i}	Transient synchronous reactances along the d axis and q axis
Z_w	Warburg impedance

References

1. Tavakoli, S.D.; Dozein, M.G.; Lacerda, V.A.; Mañe, M.C.; Prieto-Araujo, E.; Mancarella, P.; Gomis-Bellmunt, O. Grid-Forming Services From Hydrogen Electrolyzers. *IEEE Trans. Sustain. Energy* **2023**, *14*, 2205–2219. [\[CrossRef\]](#)
2. Guilbert, D.; Vitale, G. Dynamic Emulation of a PEM Electrolyzer by Time Constant Based Exponential Model. *Energies* **2019**, *12*, 750. [\[CrossRef\]](#)
3. Tuinema, B.W.; Adabi, E.; Ayivor, P.K.; García Suárez, V.; Liu, L.; Perilla, A.; Ahmad, Z.; Rueda Torres, J.L.; van der Meijden, M.A.; Palensky, P. Modelling of large-sized electrolyzers for real-time simulation and study of the possibility of frequency support by electrolyzers. *IET Gener. Transm. Distrib.* **2020**, *14*, 1985–1992. [\[CrossRef\]](#)
4. Guilbert, D.; Vitale, G. Improved Hydrogen-Production-Based Power Management Control of a Wind Turbine Conversion System Coupled with Multistack Proton Exchange Membrane Electrolyzers. *Energies* **2020**, *13*, 1239. [\[CrossRef\]](#)
5. Ghazavi Dozein, M.; Maria De Corato, A.; Mancarella, P. Fast Frequency Response Provision from Large-Scale Hydrogen Electrolyzers Considering Stack Voltage-Current Nonlinearity. In Proceedings of the 2021 IEEE Madrid PowerTech, Madrid, Spain, 28 June–2 July 2021; pp. 1–6. [\[CrossRef\]](#)
6. Dozein, M.G.; Jalali, A.; Mancarella, P. Fast Frequency Response From Utility-Scale Hydrogen Electrolyzers. *IEEE Trans. Sustain. Energy* **2021**, *12*, 1707–1717. [\[CrossRef\]](#)
7. Dozein, M.G.; De Corato, A.M.; Mancarella, P. Virtual Inertia Response and Frequency Control Ancillary Services From Hydrogen Electrolyzers. *IEEE Trans. Power Syst.* **2023**, *38*, 2447–2459. [\[CrossRef\]](#)
8. Chen, M.; Chou, S.F.; Blaabjerg, F.; Davari, P. Overview of Power Electronic Converter Topologies Enabling Large-Scale Hydrogen Production via Water Electrolysis. *Appl. Sci.* **2022**, *12*, 1906. [\[CrossRef\]](#)
9. Solanki, J.; Fröhleke, N.; Böcker, J. Implementation of Hybrid Filter for 12-Pulse Thyristor Rectifier Supplying High-Current Variable-Voltage DC Load. *IEEE Trans. Ind. Electron.* **2015**, *62*, 4691–4701. [\[CrossRef\]](#)
10. Samani, A.E.; D'Amicis, A.; De Kooning, J.D.; Bozalakov, D.; Silva, P.; Vandeveld, L. Grid balancing with a large-scale electrolyser providing primary reserve. *IET Renew. Power Gener.* **2020**, *14*, 3070–3078. [\[CrossRef\]](#)
11. Kundur, P. *Power System Stability and Control*; McGraw Hill: New York, NY, USA, 1994.
12. Hernández-Gómez, A.; Ramirez, V.; Guilbert, D.; Saldívar. Cell voltage static-dynamic modeling of a PEM electrolyzer based on adaptive parameters: Development and experimental validation. *Renew. Energy* **2021**, *163*, 1508–1522. [\[CrossRef\]](#)
13. Olivier, P.; Bourasseau, C.; Bouamama, P.B. Low-temperature electrolysis system modelling: A review. *Renew. Sustain. Energy Rev.* **2017**, *78*, 280–300. [\[CrossRef\]](#)
14. Lebbal, M.; Lecœuche, S. Identification and monitoring of a PEM electrolyser based on dynamical modelling. *Int. J. Hydrogen Energy* **2009**, *34*, 5992–5999. [\[CrossRef\]](#)

15. Hernández-Gómez, A.; Ramirez, V.; Guilbert, D. Investigation of PEM electrolyzer modeling: Electrical domain, efficiency, and specific energy consumption. *Int. J. Hydrogen Energy* **2020**, *45*, 14625–14639. [[CrossRef](#)]
16. Hernández-Gómez, A.; Ramirez, V.; Guilbert, D.; Saldivar, B. Development of an adaptive static-dynamic electrical model based on input electrical energy for PEM water electrolysis. *Int. J. Hydrogen Energy* **2020**, *45*, 18817–18830. [[CrossRef](#)]
17. Abdin, Z.; Webb, C.; Gray, E. Modelling and simulation of a proton exchange membrane (PEM) electrolyser cell. *Int. J. Hydrogen Energy* **2015**, *40*, 13243–13257. [[CrossRef](#)]
18. Martinson, C.; van Schoor, G.; Uren, K.; Bessarabov, D. Characterisation of a PEM electrolyser using the current interrupt method. *Int. J. Hydrogen Energy* **2014**, *39*, 20865–20878. [[CrossRef](#)]
19. Rubio, M.; Urquia, A.; Dormido, S. Diagnosis of PEM fuel cells through current interruption. *J. Power Sources* **2007**, *171*, 670–677. [[CrossRef](#)]
20. Garcia-Navarro, J.; Schulze, M.; Friedrich, K. Measuring and modeling mass transport losses in proton exchange membrane water electrolyzers using electrochemical impedance spectroscopy. *J. Power Sources* **2019**, *431*, 189–204. [[CrossRef](#)]
21. Mondal, D.; Chakrabarti, A.; Sengupta, A. *Power System Small Signal Stability Analysis and Control*; Elsevier: Amsterdam, The Netherlands, 2020.
22. Olivier, P. Modélisation et Analyse du Comportement Dynamique d'un Système d'Électrolyse PEM Soumis à des Sollicitations Intermittentes: Approche Bond Graph. Ph.D. Thesis, Université Lille 1, Villeneuve d'Ascq, France, 2016.
23. Rashid, M.H. *Power Electronics Handbook Devices, Circuits, and Applications*; Elsevier: Amsterdam, The Netherlands, 2011.
24. Ndiwulu, G.W.; Matalatala, M.; Lusala, A.K.; Bokoro, P.N. Distributed Hybrid Power-Sharing Control Strategy within Islanded Microgrids. In Proceedings of the 2023 31st Southern African Universities Power Engineering Conference (SAUPEC), Johannesburg, South Africa, 24–26 January 2023; pp. 1–6. [[CrossRef](#)]
25. Zacharia, L.; Asprou, M.; Kyriakides, E.; Polycarpou, M. Effect of dynamic load models on WAC operation and demand-side control under real-time conditions. *Int. J. Electr. Power Energy Syst.* **2021**, *126*, 106589. [[CrossRef](#)]
26. Pasiopoulou, I.; Kontis, E.; Papadopoulos, T.; Papagiannis, G. Effect of load modeling on power system stability studies. *Electr. Power Syst. Res.* **2022**, *207*, 107846. [[CrossRef](#)]
27. Villegas Pico, H.N.; Aliprantis, D.C.; Lin, X. *Transient Stability Assessment of Power Systems with Uncertain Renewable Generation*; Technical Report; National Renewable Energy Lab. (NREL): Golden, CO, USA, 2017.

Disclaimer/Publisher's Note: The statements, opinions and data contained in all publications are solely those of the individual author(s) and contributor(s) and not of MDPI and/or the editor(s). MDPI and/or the editor(s) disclaim responsibility for any injury to people or property resulting from any ideas, methods, instructions or products referred to in the content.